Development of Nonprecious-Metal M/N/C Electrocatalysts Prepared from π-Expanded Metal Salen Precursors

A Doctoral Dissertation
By
Yuta Tanaka

Submitted to
The Graduate School of Engineering, Osaka University
January, 2018

Acknowledgement

This study has been conducted under the direction of Professor Takashi Hayashi at the Department of Applied Chemistry, Graduate School of Engineering, Osaka University. The author would like to express his great gratitude to the supervisor, Professor Takashi Hayashi, for his suggestions, fruitful discussion and warm encouragement throughout this research. The author would like to express his sincere gratitude to Associate Professor Akira Onoda for his valuable suggestions, exciting discussion, and cordial encouragement. The author would like to deeply thank Dr. Koji Oohora for his fruitful guidance and discussions.

Acknowledgements are also made to Professor Akira Sakai, and Dr. Shotaro Takeuchi at the Department of Systems Innovation, Graduate School of Engineering Science, Osaka University, and Mr. Takao Sakata, and Professor Hidehiro Yasuda at the Research Center for ultra-high voltage electron microscopy, Osaka University, and Dr. Tomoyuki Kitano at the Analysis Technology Center, Nippon Shokubai Co., Ltd, and Mr. Yutaro Ito at the Performance Chemicals Business Division, Nippon Shokubai Co., Ltd, for their technical support on High Resolution Transmission Electron Microscope equipped with an Energy-Dispersive X-ray analyzer measurements. The author would like to specially thank Mr. Shin-ichi Okuoka at the Research Center, Nippon Shokubai Co., Ltd, and Dr. Tomoyuki Kitano at the Analysis Technology Center, Nippon Shokubai Co., Ltd, for their sincerely technical supports and suggestions for X-ray Absorption Fine Structure measurements and Extended X-ray Absorption Fine Structure analyses.

The author acknowledges Associate Professor Norimitsu Tohnai at the Department of Material and Life Science, Graduate School of Engineering, Osaka University, and Mr. Hironobu Ono at the Research Center, Nippon Shokubai Co., Ltd, for Thermogravimeter-Differential Thermal Analyzer measurements. The author thanks to Associate Professor Shinji Tamura, and Professor Nobuhito Imanaka at the Department of Applied Chemistry, Graduate School of Engineering, Osaka University, for X-ray Diffraction measurements. The author expresses their gratitude to Dr. Takashi Tsujimoto, and Professor Hiroshi Uyama at the Department of Applied Chemistry, Graduate School of Engineering, Osaka University, and Mr. Hironobu Ono at the Research Center, Nippon Shokubai Co., Ltd, for specific surface area measurements by Brunauer–Emmett–Teller theory. The author acknowledges Associate Professor Shinji Tamura, and Professor Nobuhito Imanaka at the Department of Applied Chemistry, Graduate School of Engineering, Osaka University, for Raman spectroscopy.

The author wishes to thank to Dr. Toshikazu Ono at the Department of Chemistry and Biochemistry, Graduate School of Engineering, Kyusyu University, and all the member of Hayashi Laboratory

(2012-2018) for their helpful discussion, in especially, Dr. Tsuyoshi Mashima, Dr. Hiroyuki Meichin, Mr. Ayumu Ogawa, and Ms. Kaori Oshita for their heartfelt friendship and encouragement.

Finally, the author expresses great gratitude to his family, Kazuhisa, Yukie, Miyu, Masatoshi, Hideo, Yuriko, Luke, and Moca for their incessant assistance. All the author's work here is dedicate to them.

The study was financially supported by Interactive Materials Science Cadet program (IMSC, 2013-2018), and Research Fellowship of Japan Society for the Promotion of Science for Young Scientists (16J00939, 2016-2018).

January, 2017

Yuta Tanaka

Contents

Chapter 1

General Introduction

Oxygen Reduction Reaction (ORR) in Biological Energy Conversion

Since molecular oxygen has abundantly existed on Earth from approximately 3 billion years ago, aerobic living organisms have effectively gained energy available via reduction of O_2 to sustain their lives along with respiration.[1-3] During the respiration, oxygen reduction reaction (ORR) is catalytically converted to water with four protons and four electrons smoothly, whereas non-enzymatic ORR is known to be very hard. In eukaryotes ORR is catalyzed by cytochrome *c* oxidase that locates within the inner membrane of mitochondrion (Figure 1a).[2,4-6] This enzyme contains heme iron and non-heme copper ion stabilized by three imidazole nitrogens as an active site (Figure 1b). In the process, four protons are transferred across the inner membrane of mitochondrion, helping to generate a proton gradient in the transmembrane Using this potential difference, ATP synthase is then capable of producing an ATP molecule containing a high-energy phosphate bond, which is an energy source for wide range of chemical reactions. Hence, ORR plays an important role in the generation of energy in biology.

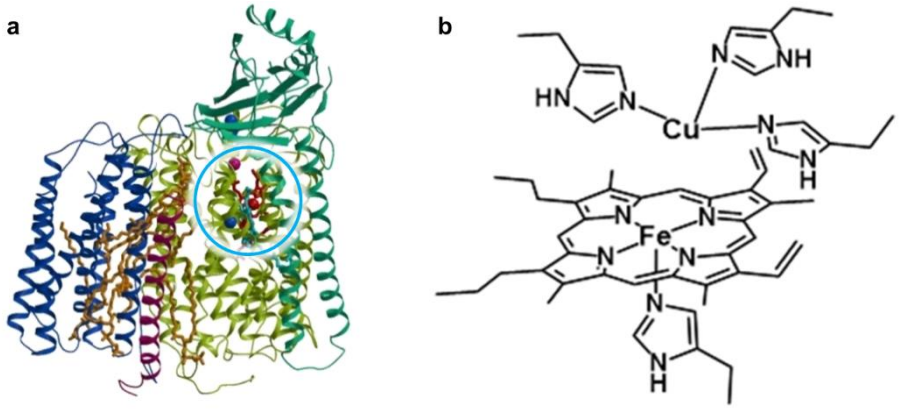

Figure 1. (a) Crystal structure of cytochrome *c* oxidase (PDB ID: 1AR1). (b) Chemical structure of heme (iron protoporphrin IX) and non-heme copper as the active site of cytochrome *c* oxidase (circle region in Figure 1a).

ORR in Artificial Energy Conversion

ORR is one of the significant chemical reactions in artificial energy conversion.[7-10] Polymer electrolyte fuel cell (PEFC) is a key energy conversion technology as an alternative to the limited energy sources such as coal, natural gas, and petroleum. PEFC consists of a two-electrode system, where electrochemical ORR proceeds in cathode, while hydrogen oxidation reaction (HOR) proceeds in anode (Figure 2).[11-15] Although this technology has received much attention as a sustainable energy source over decades, it has still faced up to one of the important issues which should require the study on a practical use. ORR consists of multiple steps involving four electrons and four protons, whereas HOR needs less steps involving two electrons. In general, electrochemical ORR requires higher overpotential because of the slow kinetics with the multiple steps. Hence it is expected that ORR needs higher energy to overcome the kinetic barrier, so-called higher overpotential.

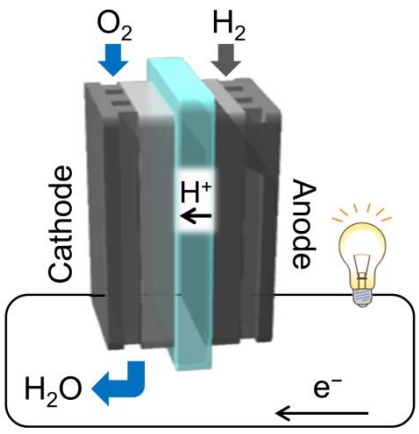

Figure 2. Schematic illustration of a polymer electrolyte fuel cell (PEFC).

Nonprecious Metal Catalysts for ORR

In the past decades, the electrocatalysts using precious metals for ORR have been extensively studied and the precious metal catalysts (PMCs) such as platinum and palladium have been designed to improve the catalytic activity including reaction rate.[16-19] The main drawback of these catalysts with precious metals requires high cost, which is not appropriate for any large scale manufacturing. The substitution of the PMCs by nonprecious metal catalysts (NPMCs) would undoubtedly decrease the cost of PEFCs for energy conversion. However, NMPCs still have a serious problem about the low catalytic activity.

NMPCs for ORR have been studied for over five decades and enormous improvements in performance

were achieved. The milestone for the development of NPMCs for ORR was reported by Jasinski in 1964, demonstrating that cobalt phthalocyanine (CoPc) is active toward ORR under alkaline conditions.[20] This finding paved a new research direction in the field of ORR catalysts, leading to tremendous investigations focusing on the employment of the transition metal macrocycle compounds as materials for ORR electrocatalysts.[21-37] These catalysts are usually immobilized on carbon supports with large surface area to provide sufficient surface area catalyzing ORR in PEFC applications. The ORR activity of these complexes has been found to be directly related to the metal ion and the ligand structure. Cobalt-based macrocyclic compounds such as CoPc and Co porphyrin have catalytic activity toward the two-electron reduction of O_2 producing H_2O_2, which is not desired for PEFC.[22,29,38-40] This reaction damages the proton exchange membrane of PEFC. In contrast, Fe-based macrocyclic compounds catalyze a four-electron ORR generating H_2O,[24,29,40] although the catalyst structures were found to decompose under acidic conditions for PEFC, resulting in a loss of the catalytic activity.

Pyrolyzed M/N/C catalysts for ORR

The breakthroughs were the findings that pyrolysis process significantly improves the activity and the stability of carbon-based NPMCs under the acidic conditions and that small molecules can be applied as a precursor for NPMC instead of more expensive metal–macrocycle compounds. Jahnke reported that the catalytic activities of NPMCs were enhanced when the catalysts are pyrolyzed at high temperature (400 ~ 1000 °C).[41] It was demonstrated that this approach is capable of generating ORR active sites containing metal and nitrogen atoms on the carbon support, which are stable under the acidic conditions.[42-46] This type of NPMCs is called a M/N/C catalyst. It has been extensively debated on transformations of the precursor structure during pyrolysis, because the atomic configuration of the transition metal macrocyclic compounds is partially or completely decomposed. The transformation of the precursor structure into the active sites has been confirmed by various methods including X-ray photoelectron spectroscopy (XPS),[47-52] Mössbauer spectroscopy,[47,48,53,54] thermogravimetric mass spectroscopy (TG-MS),[52,55] time of flight secondary ion mass spectroscopy (ToF-SIMS)[50,56-59] or extended X-ray absorption fine structure (EXAFS),[54,60] where these characterization techniques often provide further perspectives regarding the nature of atomic configurations of the M/N/C catalyst.

The synthesized M/N/C catalysts produced by pyrolysis of the simple metal complexes do not need any expensive transition metal macrocycle compounds.[61-63] Furthermore, the active sites in the catalysts could be constructed with a variety of different precursor metal complexes.

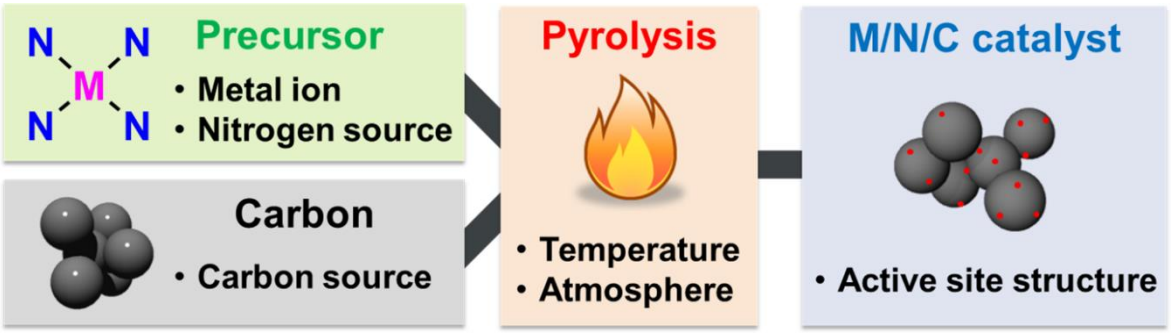

Figure 3. Schematic illustration of the optimization process for the development of M/N/C catalysts.

In 1986, Yeager *et al.* reported that the requirement was construction of a proper metal–nitrogen coordination in M/N/C catalysts resulting from pyrolysis.[55] They achieved to synthesize ORR active catalyst materials using simple metal salts, nitrogen and carbon precursor materials. Since this report, several ORR active M/N/C catalysts were successfully prepared by inexpensive polymer materials, such as polyacrylonitrile (PAN) and polyaniline (PANI) with Co or Fe salts, and carbon supports.[61,64-66] This opened a new direction of the research involving inexpensive precursor materials.

Nowadays, besides the inexpensive industrial materials, a biomaterial catalyst has been employed as a precursor for a M/N/C catalyst, such as plant leaves[67] and seaweeds[68]. They contain iron and nitrogen, which are essential elements of precursors for M/N/C catalysts, as nutrients for their growth. These biomaterials are regarded as a natural biomass that rapidly regrows and is environmentally friendly. Synthesis of an economically reasonable M/N/C catalysts derived from natural resources such as biomaterials is therefore an attractive investigation and still challenging. To this end, the author has focused on developing a M/N/C catalyst using a unique biomaterial, myoglobin, which consists of heme iron and nitrogen-rich protein matrix, and abundant in the muscle tissues of mammals (Chapter 1).

These discoveries that the active M/N/C catalysts for ORR are generated by the pyrolysis of a mixture of precursor materials containing transition metal, nitrogen, and carbon, have provided the way for extensive investigation of a variety of precursors. For the development of M/N/C catalysts enabling high catalytic activity and stability under PEFC operating conditions, the optimization of precursor materials, pyrolysis conditions, and catalyst structures has been focused with systematic trials and error investigations (Figure 3). Several factors have been presumed to be significant for the activity and stability of pyrolyzed M/N/C catalysts; types of transition metals, pyrolysis conditions, surface properties of carbon support, and nitrogen content. Extensive progresses over recent years have been achieved in clarifying these factors. Although several M/N/C catalysts have been reported to be highly active in electrocatalytic ORR exceeding

that of platinum catalysts, the comprehensive understanding of the active sites in M/N/C catalysts is still limited.

Proposed Active Sites (M–N_4/C structure)

The bottleneck of development of pyrolyzed M/N/C catalysts is due to indistinctness of the actual active site structures. In the case of non-pyrolyzed transition metal macrocycle compounds, the well-designed structure is remained during synthesis procedures. This enables a direct correlation between the catalyst structures and the ORR activity of the resulting catalyst. On the other hand, in the case of M/N/C catalysts pyrolyzed at high temperature, the structures of the precursors are partially or completely altered, thereby remaining uncertainties about the nature of the active sites and the mechanism of ORR.

In terms of the nature of the active sites in the ORR catalysts, several different structures and formation mechanisms have been proposed. Dodelet *et al.* synthesized a M/N/C catalyst prepared from a mixture of phenanthroline and iron salts on carbon support.[69] Through ToF-SIMS, they proposed that the Fe–N_4/C active sites containing an iron ion coordinated by four pyridinic nitrogen configuration bound to the edges of graphitic sheets of the carbon supports (Figure 4a). This proposal coincides with Yeager's claim on the role of transition metals in carbon-based catalysts. Yeager *et al.* asserted the outcomes of their polyacrylonitrile-based catalyst (PAN/Fe or Co) and demonstrated that the addition of transition metals such as Fe and Co to nitrogen-doped carbon structures promotes the generation of pyridinic nitrogen as binding sites for the transition metal ions generating the active sites for ORR.[55,61]

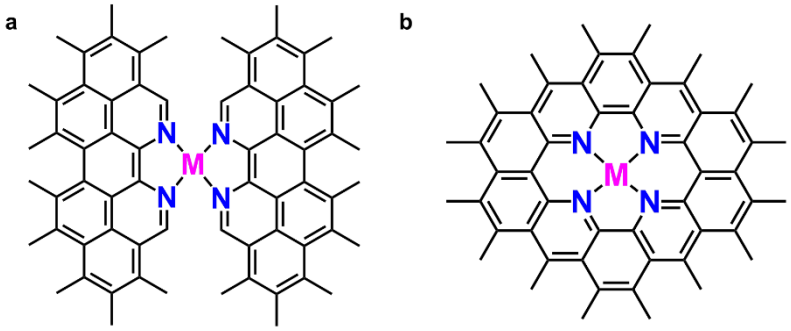

Figure 4. Proposed active site structure (M–N_4/C structure) of M/N/C catalysts by (a) J. P. Dodelet *et al.*, and (b) S. Mukerjee *et al.*

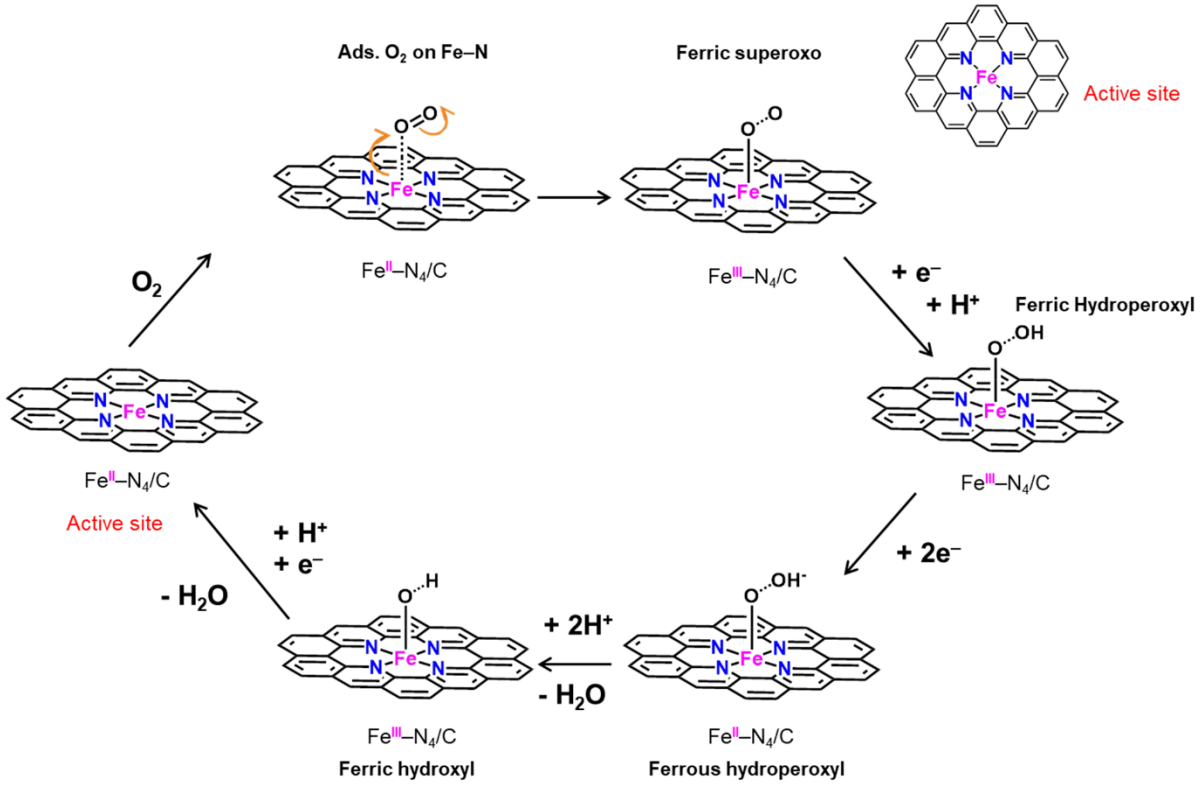

Figure 5. Proposed ORR mechanistic pathways on M–N_4/C structure.

Mukerjee *et al*. synthesized a M/N/C catalyst prepared from a mixture of poly(*N*-vinylguanidine) and iron salts on carbon support. Using *in situ* electrochemical X-ray absorption spectroscopy, they proposed that the covalent integration of the Fe–N_x sites is embedded within the π-conjugated carbon basal plane in the form of Fe–N_x/C (Figure 4b), and the ORR mechanism with the Fe–N_x/C structure (Figure 5).[70] Furthermore, Zelenay *et al.* identified the Fe–N_x/C structures in the catalyst prepared from a mixture of cyanamide, polyaniline, and iron salts on the carbon support by STEM-EELS.[71] Despite of such an extensive investigation, none of them has reached at the detection of the actual active site structure.

The author assumed that the structural determination of the ORR active site and elucidation of the forming process are crucial for the improvement of the electrochemical activities of M/N/C catalysts. Toward this goal, the development of an unprecedented method for the construction of the ORR active sites is needed. In this aspect, previous investigations have focused on precursor materials. Tang *et al.* reported that the M/N/C catalysts synthesized from a mixture of cobalt porphyrins tethering *p*-methoxyphenyl group, or *p*-trifluorophenyl group at four *meso* positions, and carbon supports have similar electrocatalytic performance in ORR.[54] Since the substitution at *meso* positions does not affect the catalytic activity, it was demonstrated that the structure of the active sites during pyrolysis relies on the macrocyclic frameworks of

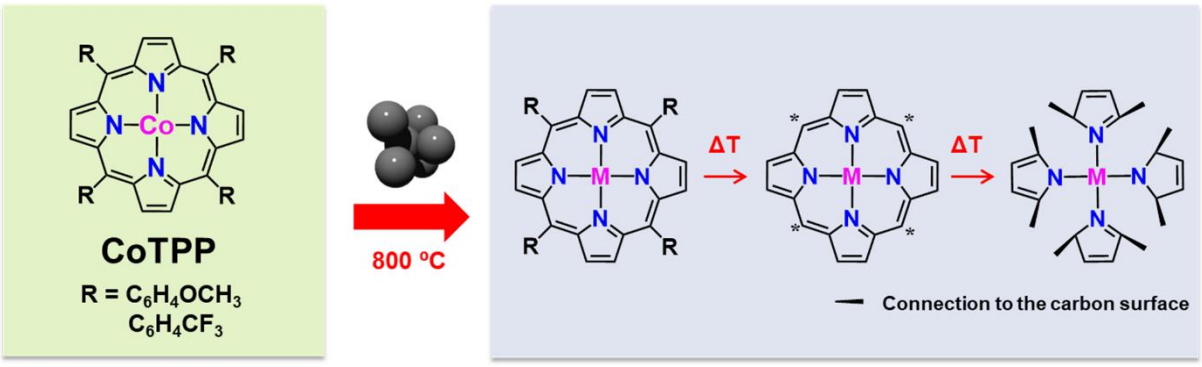

Figure 6. Proposed decomposition mechanism of the cobalt porphyrins with carbon supports during pyrolysis.

the precursors. They also concluded that the decomposition of precursors progressed in the similar manner, and that the similar active site structure was constructed in the case of macrocyclic compound precursors (Figure 6). On the other hand, Roncaroli *et al.* reported that the M/N/C catalysts synthesized from different nitrogen-containing organic compounds as a nitrogen source precursor exhibited different ORR activities.[72] This suggests that the chemical structure and the thermal stability of the precursor contribute to the construction of the active sites and ORR performances.

The author, therefore, focused on the design of the precursor framework structures in order to clarify the influence of the precursor structure on the formation of the active sites and the ORR activity. He employed a salen complex as a catalyst precursor because the synthesis is easy due to the simple structure.[41,73] In addition, it is possible to alter and diversify the peripheral structure of the metal complex precersor. Introduction of aromatic rings was examined to modify the periphery of the salen complex framework. Because the aromatic rings impart thermal stability to the salen complex, they are expected to be incorporated and fused into the carbon supports via annulation during the pyrolysis (Figure 7). On the basis of this strategy, the author developed the nonprecious metal M/N/C catalysts synthesized from π-expanded metal salen precursors with several different types of transition metal-ion centers for improvement of the electrochemical activities (Chapter 2 and 3).

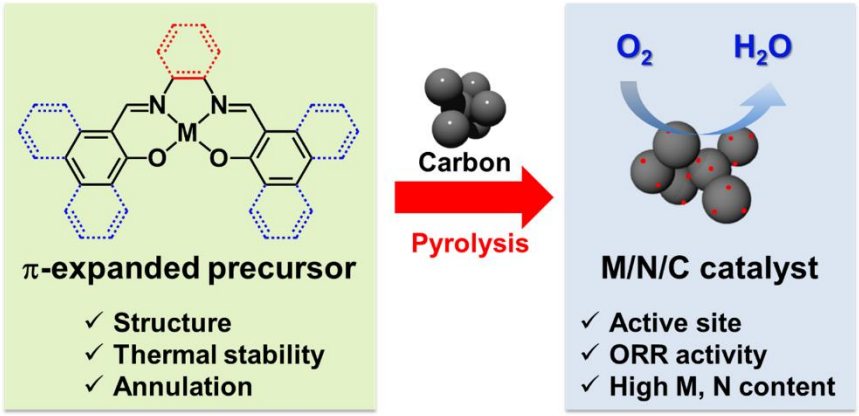

Figure 7. Schematic illustration for the development of M/N/C catalysts synthesized from π-expanded salen precursors.

Outline of This Thesis

Chapter 1

M/N/C catalysts derived from biomaterials were developed using myoglobin (Mb) containing a heme with Fe and nitrogen atoms and a nitrogen-rich protein matrix as a precursor. The Mb-based M/N/C catalysts (Mb@VC) prepared from a mixture of Mb and carbon supports by pyrolysis were investigated. Mb@VC catalysts pyrolyzed at 940 °C have the highest electrochemical ORR activity under acidic conditions with the efficient four-electron reduction of O_2.

Chapter 2

A new method by systematically tuning an aromatic framework of Fe salen complex precursors to improve the ORR activity of the M/N/C catalyst was developed. Aromatic moieties attached to Fe salen derivatives impart higher thermal stability to alter an annulation process of the precursors during pyrolysis. The author describes the preparation and characterization of the Fe/N/C ORR catalysts via pyrolysis of the π-expanded Fe salen complexes and their ORR activities in Chapter 2. It is found that tuning the ligand structure of precursors leads to a remarkable enhancement of ORR activity and an increase in efficiency of the four-electron reduction process during ORR of the pyrolyzed Fe/N/C catalysts.

Chapter 3

Monometallic M/N/C catalysts and bimetallic FeM/N/C catalysts containing different types of transition metal (Fe, Cu, Co, Ni, and Mn) were prepared from thermally stable π-expanded metal salen complexes. The preparation and characterization of the complexes and the measurement of their ORR activities are described in Chapter 3. It is found that combining the π-expanded metal salen precursors, in particular Fe and Cu, results in a significant improvement of the ORR performace including four-electron reduction selectivity of the pyrolyzed bimetallic FeM/N/C catalysts.

Reference and Notes

1. S. Arnold and B. Kadenbach, *Eur. J. Biochem.*, 1997, **249**, 350–354.
2. V. R. I. Kaila, M. I. Verkhovsky and M. Wikström, *Chem. Rev.*, 2010, **110**, 7062–7081.
3. E. Balsa, R. Marco, E. Perales-Clemente, R. Szklarczyk, E. Calvo, M. Landázuri and J. A. Enríquez, *Cell Metabolism*, 2012, **16**, 378–386.
4. T. Tsukihara, H. Aoyama, E. Yamashita, T. Tomizaki, H. Yamaguchi, K. Shinzawa-Itoh, R. Nakashima, R. Yaono and S. Yoshikawa, *Science*, 1995, **269**, 1069–1074.
5. T. Tsukihara, H. Aoyama, E. Yamashita, T. Tomizaki, H. Yamaguchi, K. Shinzawa-Itoh, R. Nakashima, R. Yaono and S. Yoshikawa, *Science*, 1996, **272**, 1136−1144.
6. S. Yoshikawa, K. Shinzawa-Itoh, R. Nakashima, R. Yaono, E. Yamashita, N. Inoue, M. Yao, M. J. Fei, C. P. Libeu, T. Mizushima, H. Yamaguchi, T. Tomizaki and T. Tsukihara, *Science*, 1998, **280**, 1723−1729.
7. M. K. Debe, *Nature*, 2012, **486**, 43−51.
8. R. Cao, J.-S. Lee, M. Liu and J. Cho, *Adv. Energy Mater.*, 2012, **2**, 816–829.
9. Q. Li, R. Cao, J. Cho and G. Wu, *Adv. Energy Mater.*, 2014, **4**, 1301415.
10. D. Higgins, P. Zamani, A. Yu and Z. Chen, *Energy Environ. Sci.*, 2016, **9**, 357−390.
11. L. Carrette, K. A. Friedrich and U. Stimming, *Fuel Cells*, 2001, **1**, 5–39.
12. A. S. Arico, S. Srinivasan and V. Antonucci, *Fuel Cells*, 2001, **1**, 133–161.
13. M. R. Palacin, *Chem. Soc. Rev.*, 2009, **38**, 2565–2575.
14. J. Suntivich, H. A. Gasteiger, N. Yabuuchi, H. Nakanishi, J. B. Goodenough and Y. Shao-Horn, *Nat. Chem.*, 2011, **3**, 546.
15. F. Cheng and J. Chen, *Chem. Soc. Rev.*, 2012, **41**, 2172–2192.
16. J. Snyder, T. Fujita, M. W. Chen and J. Erlebacher, *Nat. Mater.*, 2010, **9**, 904−907.
17. A. Rabis, P. Rodriguez and T. J. Schmidt, *ACS Catal.*, 2012, **2**, 864−890.
18. M. Shao, Q. Chang, J.-P. Dodelet and R. Chenitz, *Chem. Rev.*, 2016, **116**, 3594−3657.
19. T. Mittermeier, A. Weiß, H. A. Gasteiger and F. Hasché, *J. Electrochem. Soc.*, 2017, **164**, F1081–F1089.
20. R. Jasinski, *Nature*, 1964, **201**, 1212–1213.
21. J. A. R. van Veen and C. Visser, *Electrochim. Acta*, 1979, **24**, 921–928.
22. K. Wiesener, D. Ohms, V. Neumann and R. Franke, *Mater. Chem. Phys.*, 1989, **22**, 457–475.
23. S. Baranton, C. Coutanceau, E. Garnier and J. M. Léger, *J. Electroanal. Chem.*, 2006, **590**, 100–110.
24. S. Baranton, C. Coutanceau, C. Roux, F. Hahn and J. M. Léger, *J. Electroanal. Chem.*, 2005, **577**, 223–234.
25. C. Shi and F. C. Anson, *Inorg. Chem.*, 1990, **29**, 4298–4305.
26. G. I. Cárdenas-Jirón, *J. Phys. Chem. A*, 2002, **106**, 3202–3206.

27. J. Ouyang, K. Shigehara, A. Yamada and F. C. Anson, *J. Electroanal. Chem. Interfacial Electrochem.*, 1991, **297**, 489–498.
28. E. Song, C. Shi and F. C. Anson, *Langmuir*, 1998, **14**, 4315–4321.
29. P. Vasudevan, S. N. Mann and S. Tyagi, *Transition Met. Chem.*, 1990, **15**, 81–90.
30. L. Zhang, C. Song, J. Zhang, H. Wang and D. P. Wilkinson, *J. Electrochem. Soc.*, 2005, **152**, A2421–A2426.
31. K. M. Kadish, L. Frémond, Z. Ou, J. Shao, C. Shi, F. C. Anson, F. Burdet, C. P. Gros, J.-M. Barbe and R. Guilard, *J. Am. Chem. Soc.*, 2005, **127**, 5625–5631.
32. N. Kobayashi, P. Janda and A. B. P. Lever, *Inorg. Chem.*, 1992, **31**, 5172–5177.
33. C. Shi, B. Steiger, M. Yuasa and F. C. Anson, *Inorg. Chem.*, 1997, **36**, 4294–4295.
34. C. Song, L. Zhang, J. Zhang, D. P. Wilkinson and R. Baker, *Fuel Cells*, 2007, **7**, 9–15.
35. B. Steiger and F. C. Anson, *Inorg. Chem.*, 1997, **36**, 4138–4140.
36. R. Baker, D. P. Wilkinson and J. Zhang, *Electrochim. Acta*, 2008, **53**, 6906–6919.
37. H. Liu, L. Zhang, J. Zhang, D. Ghosh, J. Jung, B. W. Downing and E. Whittemore, *J. Power Sources*, 2006, **161**, 743–752.
38. A. B. Solovieva and S. F. Timashev, *Russ. Chem. Rev.*, 2003, **72**, 965–984.
39. J. H. Zagal, *Coord. Chem. Rev.*, 1992, **119**, 89–136.
40. Z. Shi and J. Zhang, *J. Phys. Chem. C*, 2007, **111**, 7084–7090.
41. H. Jahnke, M. Schönborn and G. Zimmermann, *Top. Curr. Chem.*, 1976, **61**, 133−181.
42. J.-i. Ozaki, S.-i. Tanifuji, A. Furuichi and K. Yabutsuka, *Electrochim. Acta*, 2010, **55**, 1864–1871.
43. C. Médard, M. Lefèvre, J. P. Dodelet, F. Jaouen and G. Lindbergh, *Electrochim. Acta*, 2006, **51**, 3202–3213.
44. F. Jaouen, S. Marcotte, J.-P. Dodelet and G. Lindbergh, *J. Phys. Chem. B*, 2003, **107**, 1376–1386.
45. D. Villers, X. Jacques-Bédard and J.-P. Dodelet, *J. Electrochem. Soc.*, 2004, **151**, A1507–A1515.
46. F. Jaouen, F. Charreteur and J. P. Dodelet, *J. Electrochem. Soc.*, 2006, **153**, A689–A698.
47. J. Blomquist, H. Lang, R. Larsson and A. Widelov, *J. Chem. Soc., Fraday Trans.*, 1992, **88**, 2007–2011.
48. U. I. Kramm, I. Abs-Wurmbach, I. Herrmann-Geppert, J. Radnik, S. Fiechter and P. Bogdanoff, *J. Electrochem. Soc.*, 2011, **158**, B69–B78.
49. G. Liu, X. Li, P. Ganesan and B. N. Popov, *Electrochim. Acta*, 2010, **55**, 2853–2858.
50. G. Lalande, G. Faubert, R. Côté, D. Guay, J. P. Dodelet, L. T. Weng and P. Bertrand, *J. Power Sources*, 1996, **61**, 227–237.
51. P. Gouérec, M. Savy and J. Riga, *Electrochim. Acta*, 1998, **43**, 743–753.
52. Y. Nabae, S. Moriya, K. Matsubayashi, S. M. Lyth, M. Malon, L. Wu, N. M. Islam, Y. Koshigoe, S. Kuroki, M.-a. Kakimoto, S. Miyata and J.-i. Ozaki, *Carbon*, 2010, **48**, 2613–2624.
53. U. I. Koslowski, I. Abs-Wurmbach, S. Fiechter and P. Bogdanoff, *J. Phys. Chem. C*, 2008, **112**, 15356–15366.

54. A. L. Bouwkamp-Wijnoltz, W. Visscher, J. A. R. van Veen, E. Boellaard, A. M. van der Kraan and S. C. Tang, *J. Phys. Chem. B*, 2002, **106**, 12993–13001.
55. D. Scherson, A. A. Tanaka, S. L. Gupta, D. Tryk, C. Fierro, R. Holze, E. B. Yeager and R. P. Lattimer, *Electrochim. Acta*, 1986, **31**, 1247–1258.
56. G. Faubert, G. Lalande, R. Côté, D. Guay, J. P. Dodelet, L. T. Weng, P. Bertrand and G. Dénès, *Electrochim. Acta*, 1996, **41**, 1689–1701.
57. M. Lefèvre, J. P. Dodelet and P. Bertrand, *J. Phys. Chem. B*, 2002, **106**, 8705–8713.
58. M. Lefèvre, J. P. Dodelet and P. Bertrand, *J. Phys. Chem. B*, 2005, **109**, 16718–16724.
59. L. T. Weng, P. Bertrand, G. Lalande, D. Guay and J. P. Dodelet, *Appl. Surf. Sci.*, 1995, **84**, 9–21.
60. B. van Wingerden, J. A. R. van Veen and C. T. J. Mensch, *J. Chem. Soc., Fraday Trans.*, 1988, **84**, 65–74.
61. S. Gupta, D. Tryk, I. Bae, W. Aldred and E. Yeager, *J. Appl. Electrochem.*, 1989, **19**, 19–27.
62. M. C. M. Alves, J. P. Dodelet, D. Guay, M. Ladouceur and G. Tourillon, *J. Phys. Chem.*, 1992, **96**, 10898–10905.
63. D. Ohms, S. Herzog, R. Franke, V. Neumann, K. Wiesener, S. Gamburcev, A. Kaisheva and I. Iliev, *J. Power Sources*, 1992, **38**, 327–334.
64. G. Wu, K. L. More, C. M. Johnston and P. Zelenay, *Science*, 2011, **332**, 443–447.
65. G. Wu, N. H. Mack, W. Gao, S. Ma, R. Zhong, J. Han, J. K. Baldwin and P. Zelenay, *ACS Nano*, 2012, **6**, 9764–9776.
66. M. Ferrandon, A. J. Kropf, D. J. Myers, K. Artyushkova, U. Kramm, P. Bogdanoff, G. Wu, C. M. Johnston and P. Zelenay, *J. Phys. Chem. C*, 2012, **116**, 16001–16013.
67. L. Y. Zhang, Z. Zhou, Z. Liu and C. M. Li, *ChemElectroChem*, 2016, **3**, 1466–1470.
68. M. Y. Song, H. Y. Park, D.-S. Yang, D. Bhattacharjya and J.-S. Yu, *ChemSusChem*, 2014, **7**, 1755–1763.
69. M. Lefèvre, E. Proietti, F. Jaouen and J.-P. Dodelet, *Science*, 2009, **324**, 71−74.
70. U. Tylus, Q. Jia, K. Strickland, N. Ramaswamy, A. Serov, P. Atanassov and S. Mukerjee, *J. Phys. Chem. C*, 2014, **118**, 8999–9008.
71. H. T. Chung, D. A. Cullen, D. Higgins, B. T. Sneed, E. F. Holby, K. L. More and P. Zelenay, *Science*, 2017, **357**, 479–484.
72. F. Roncaroli, E. S. Dal Molin, F. A. Viva, M. M. Bruno and E. B. Halac, *Electrochim. Acta*, 2015, **174**, 66–77.
73. J. Du, F. Cheng, S. Wang, T. Zhang and J. Chen, *Scientific Reports*, 2014, **4**, 4386.

Chapter 1

Myoglobin-based non-precious metal carbon catalysts for an oxygen reduction reaction

1-1. Introduction

Polymer electrolyte fuel cells (PEFCs) currently represent one of the most promising technologies for energy conversion. It is desirable to replace the Pt catalysts used at both of the fuel cell electrodes with non-precious metal catalysts (NPMCs).[1] In particular provision of an NPMC cathodic catalyst for the oxygen reduction reaction (ORR) would be expected to drive the development of new PEFCs. The envelopment of NPMCs with high ORR activity has thus been a focal point of PEFC studies. Since Jasinski discovered that a simple metal-N_4 complex, cobalt phthalocyanine, catalyzes an ORR[2], other CoN_4- and FeN_4 macrocycles have been found to be suitable for use as ORR catalysts.[3] The stability and activity of a series of macrocycle-based carbon catalysts were then significantly improved after heat treatment between 500 and 900 °C under an inert atmosphere.[4-17] Promising NPMCs synthesized from a metal ion, a source of carbon, and a source of nitrogen atom by heat treatment have been reported.[18-22]

Natural N_4-macrocyclic metal complexes such as heme (iron protoporphyrin IX) are used in the actives site of a wide range of enzyme-driven redox reactions.[23] In particular, cytochrome *c* oxidase contains heme in the active site and catalyzes an ORR in conjunction with a neighboring Cu site.[24-26] Model complexes and biomimetic models including a heme cofactor have thus been studied to unravel the intriguing four-electron reduction process.[27-32] Heme has also been recognized as an attractive building block for construction of NPMCs because they are easily obtained from natural sources. Several groups have reported the preparation of hemin-based NPMCs and investigated their electrocatalytic activity.[33,34] Direct carbonization from a hemoprotein is expected to be advantageous. Maruyama *et al.* reported that NPMCs prepared from hemoproteins such as catalase and hemoglobin have ORR activity.[35-37] Our group has been engaged in engineering of myoglobin (Mb), another representative hemoprotein (Figure 1-1)[38-43] which has not yet been explored as a possible NPMC precursor. Herein, the author report the characterization of

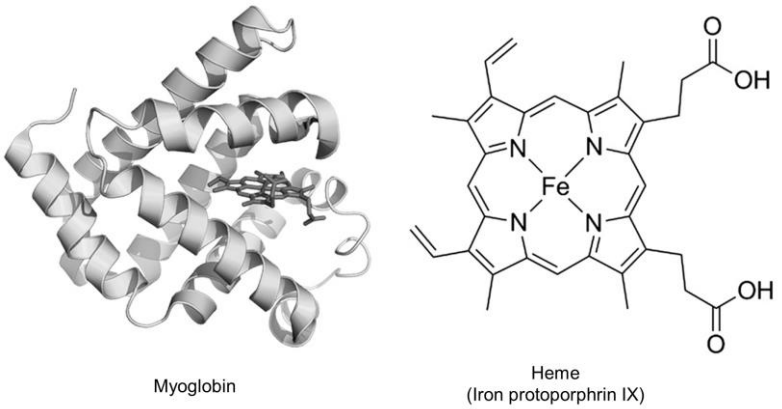

Figure 1-1. Crystal structure of horse heart myoglobin (PDB ID: 1WLA) and chemical structure of heme (iron protoporphrin IX).

NPMCs prepared from Mb by heat treatment and an investigation of the ORR activity of these NPMCs under acidic conditions.

1-2. Results and Discussion

Characterization of Mb-based NPMC by XRD

The turbostratic structure with random layers of a graphitic lattice in the Mb@VC catalyst pyrolyzed at 940 °C was analyzed by X-ray diffraction (XRD) as shown in Figure 1-2. In general, powder samples of carbons in a turbostratic structure provide diffraction peaks for 002 (2θ = 25.5~26.6°), 004 (2θ = 53.2~54.7°), and a two-dimensional 10 line at *ca*. 44°. Previous XRD analyses on carbonized materials of catalase and hemoglobin showing two broad peaks at *ca*. 25° and 44° confirmed the amorphous structure of the materials.[35, 36] The Mb@VC catalyst was found to exhibit a strong and broad peak at *ca*. 25° and very weak peak at 44°. These observations confirm the turbostratic and amorphous structure. Heat treatment of the iron-containing precursor often generates Fe_2O_3, which is identified by diffraction at 35°. The absence of the peak assignable to Fe_2O_3 suggests that Fe_2O_3 is not included in the Mb@VC catalyst pyrolyzed at 940 °C, which was washed with an acidic solution.

Raman spectroscopy

Raman spectroscopic analysis provides valuable information on the microstructure of carbon materials. It is known that highly ordered graphite presents a band between 1100 and 1700 cm^{-1}, whereas disordered carbons show significantly different spectra with a D (disorder) band in the vicinity of 1350 cm^{-1} and graphitized carbons give rise to a G (graphite) band at 1580 cm^{-1}, which is assignable to in-plane

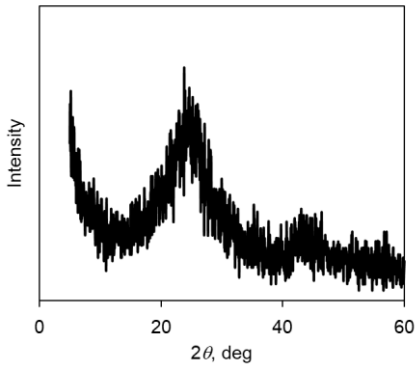

Figure 1-2. X-ray diffraction spectrum of the Mb@VC catalyst pyrolyzed at 940 ºC.

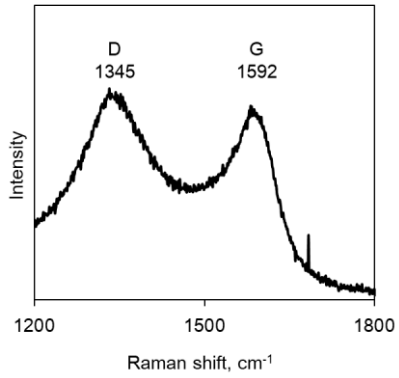

Figure 1-3. Raman spectrum of the Mb@VC catalyst pyrolyzed at 940 ºC.

displacement of the carbons strongly coupled in the hexagonal sheets.[44, 45] The Raman spectrum of the carbonized Mb presenting typical D- and G-bands indicates that the disordered carbonous structure is included in the catalyst (Figure 1-3). The microcrystalline planar crystal size (La) was calculated from *I*(D) and *I*(G), which represent the integrated intensities of D and G bands, respectively (Equation 1-1).[44, 45]

$$L_a = 44[I(\mathrm{D})/I(\mathrm{G})]^{-1} \quad (1\text{-}1)$$

From Equation 1-1, the *L*a value was estimated to be 1.9 nm for the Mb-based catalyst. The small *L*a value indicates that the crystalline domain does not grow sufficiently and that the amorphous domain is abundant in the catalysts.

XPS

The XPS analysis for the N1s state was performed to determine the chemical structure of the nitrogen containing graphitic layer (Figure 1-4). Previous experimental and theoretical studies reported that three

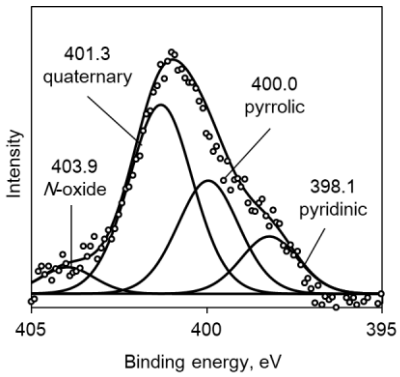

Figure 1-4. N1s XPS spectrum of the Mb@VC catalyst pyrolyzed at 940 ºC (Circles). The deconvoluted spectra are shown.

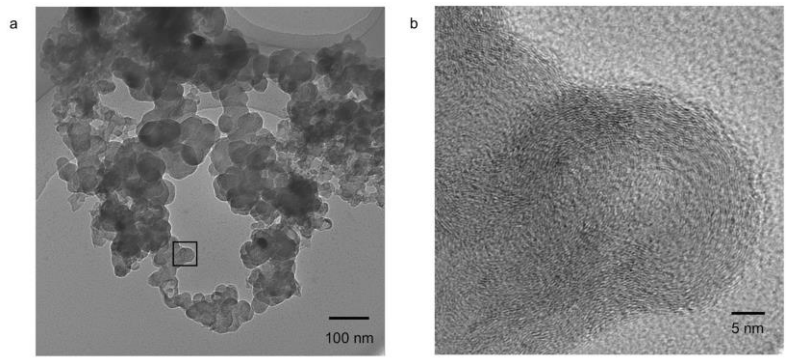

Figure 1-5. (a) TEM image of the Mb@VC catalyst pyrolyzed at 940 ºC. (b) HR-TEM image of the boxed region in Figure 1-5a.

types of nitrogen atoms appear as the N1s peak in the range of 398 and 403 eV binding energy.[46-48] The N1s peak at 398.3–399.5 eV is assigned to the pyridinic N atom at the edge of a graphene layer and the peak at 399.9–400.7 eV is assigned to the pyrrolic N atom. The N1s peak at 401– 403 eV is assigned to the graphitic nitrogen atom bound to three carbon atoms. Therefore, after the heat treatment, the Mb@VC catalysts were found to predominantly contain the pyridinic and pyrrolic N atoms in the carbon framework (Figure 1-4), which would remain to provide a binding site for the iron atom.

TEM

TEM images of the Mb@VC catalyst synthesized after the heat treatment at 940 ℃ are shown in Figure 1-5a. The graphitic nanostructures are formed on the carbon aggregate after the carbonization of protoporphyrin embedded within the Mb protein matrix (Figure 1-5b). In addition, large iron oxide aggregates were rarely observed, suggesting that the iron atoms are well-dispersed and embedded as the Fe

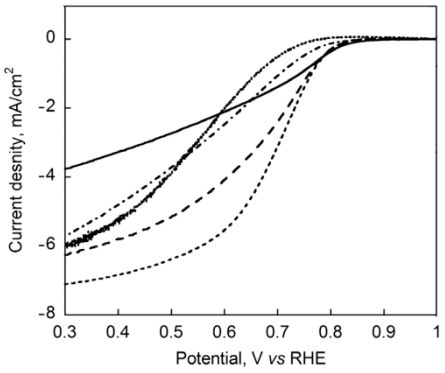

Figure 1-6. Polarization curves of Mb@VC catalysts synthesized at different temperatures of 740 °C (solid line), 840 °C (long dashed line), 940 °C (dashed line), 1040 °C (dot dashed line), and 1140 °C (dotted line) coated on GCE in O_2 saturated 0.1 M $HClO_4$ solution. Scan rate:10 mV/s. Rotation rate: 2000 rpm.

active sites within the carbon surface. Therefore, the myoglobin matrix could contribute to dispersal of the Fe macrocycle moieties on the carbon structures.

Electrochemical performance of ORR

The ORR activities of the different samples of Mb-based carbon catalysts synthesized by heat treatment at 740, 840, 940, 1040, and 1140 °C were analyzed by hydrodynamic voltammetry. The Mb@VC catalyst was suspended in a Nafion solution/isopropanol solution and the catalyst ink was immobilized on the GCE. This electrode was used as a working electrode in the RDE experiments in an O_2-saturated 0.1 M $HClO_4$ solution. The measured current was subtracted from the background current under an N_2-saturated atmosphere. The polarization curves of the catalysts are shown in Figure 1-6. The ORR activity of the catalyst was also analyzed by hydrodynamic voltammetry under the similar conditions at different rotating rates (Figure 1-7), and the results were analyzed using the Koutecky–Levich equation (Equations 1-2 and 1-3).[49]

$$I^{-1} = I_K^{-1} + I_L^{-1} \qquad (1\text{-}2)$$

$$I_L = 0.620\, nFAD_0^{2/3}\omega^{1/2}\nu^{-1/6}C_0 \qquad (1\text{-}3)$$

where I, I_K, and I_L represent the measured, kinetically-controlled, and diffusion-limited currents, respectively. ω is the electrode rotation rate, n is the overall number of electrons transferred in the half reaction, F is the Faraday constant (96,485 C.mol^{-1}), C_0 is the bulk concentration of O_2 dissolved in the electrolyte (1.18 × 10-6 mol.cm^{-3}), A is the electrode surface (0.196 cm^2), D_0 is the O_2 diffusion coefficient (1.9 × 10^{-5} cm^2.s^{-1}), and ν is the kinematic viscosity of the electrolyte (9.87 × 10^{-3} cm^2.s^{-1}). The plot of the

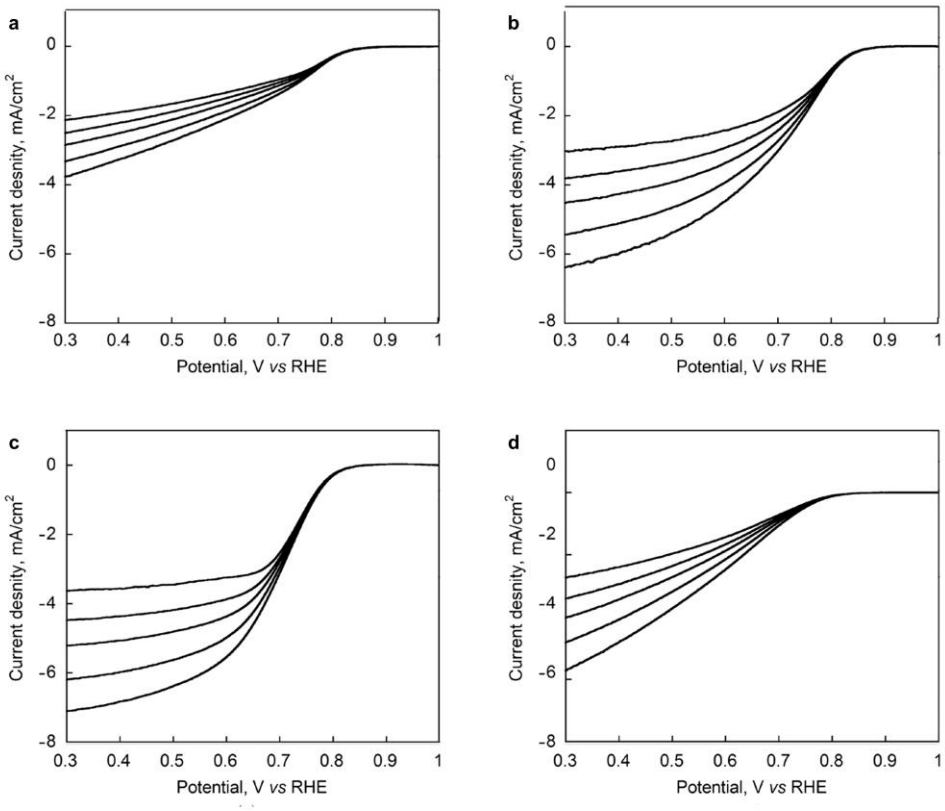

Figure 1-7. Polarization curves of Mb@VC catalysts synthesized at (a) 740 °C, (b) 840 °C, (c) 940 °C, and (d) 1040 °C coated on GCE in O_2 saturated 0.1 M $HClO_4$ solution with different rotation rates of 600, 900, 1200, 1600, 2000 rpm. Scan rate: 10 mV/s.

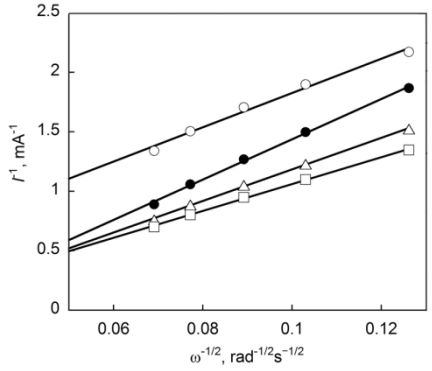

Figure 1-8. Koutecky-Levich plots at 0.3 V for the Mb@VC catalysts synthesized at different temperatures of 740 °C(circles), 840 °C (triangles), 940 °C (squares), and 1040 °C (filled circles).

inverse of the current *vs.* $\omega^{-1/2}$ yields a straight line with the intercept corresponding to I_K and the slopes reflecting the I_L, which was used to calculate the number of electrons involved in the ORR (Figure 1-8).

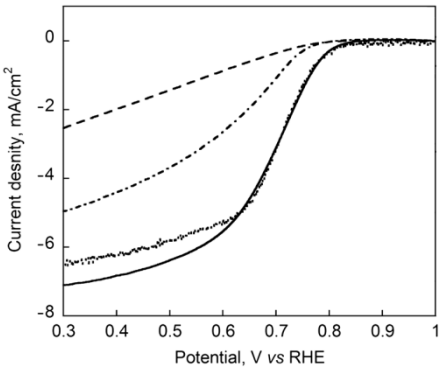

Figure 1-9. Polarization curves of the catalysts synthesized from apoMb (dashed line), heme (dotted line), Co-substituted Mb (dash dotted line), and Mb (solid line) at 940 °C coated on GCE in O_2 saturated 0.1 M $HClO_4$ solution. Scan rate: 10 mV/s. Rotation rate: 2000 rpm.

The results on the polarization curve show that the ORR activity is dependent on the pyrolytic temperature: (i) The ORR activity increases as the heat-treatment temperature increases until 940 ℃; (ii) the highest catalytic activity is obtained for the sample produced at 940 ℃; (iii) samples produced at higher temperatures (> 940 ℃) have decreased activity in terms of the onset potential and the current density; (iv) the Koutecky–Levich equation indicates that the Mb-based catalysts synthesized at 940 ℃ have the highest activity for four-electron ORR (n = *ca*. 4) the n values for the catalysts produced at other temperatures are 3.6 at 740 ℃, 3.7 at 840 ℃, and 2.9 at 1040 ℃; and (v) the ORR catalyzed by Mb@VC prepared at 940 ℃ is diffusion-controlled at a lower potential than 0.3 V (*vs.* RHE) and the onset potential is 0.84 V. The decrease in the activity for the samples prepared at higher temperatures would derive from the loss of the active sites.[36]

To determine the effective component in the source materials of the pyrolyzed catalyst, Mb@VC, the ORR activities of two catalysts were evaluated; the catalyst pyrolyzed from an apo form of Mb (apoMb) in which the heme was removed (apoMb@VC) and the catalyst pyrolyzed from heme without the Mb matrix (heme@VC) (Figure1-9). The apoMb@VC catalyst clearly showed lower ORR activity, while the heme@VC catalyst showed high activity similar to that of Mb@VC. In addition, the heme@VC catalyst efficiently catalyzes four-electron reduction of O_2. These results suggest that the key component required for high ORR activity is derived from the carbonized Fe−N_x species pyrolyzed from the heme moiety. The author also investigated cobalt-substituted Mb, which was prepared by the reconstitution of apoMb with cobalt protoporphyrin IX as a source of NPMC (CoMb@VC). Although the number of electron (n) involved in the ORR of CoMb@VC (n = 3.1) is higher than that of the metal-free catalyst, apoMb@VC, it is lower relative to the Mb@VC containing Fe.

1-3. Conclusions

The author developed a high performance NPMC for four-electron ORR, which is appropriate for use at the cathode in PEFCs. Myoglobin, which contains heme, a natural iron N_4-macrocyclic cofactor is used as the catalyst source. It is found that the Mb-based NPMC pyrolyzed at 940 °C has the highest activity toward four-electron ORR with an onset potential of 0.84 V. This study demonstrates that myoglobin has excellent potential for use as a precursor of NPMCs in construction of PEFCs.

1-4. Experimental Section

Materials and methods

Carbon black (Vulcan XC72R) (VC) was purchased from MOUBIC INC. Horse heart myoglobin was purchased from Sigma-Aldrich. Myoglobin was dissolved in water and the precipitates were removed by centrifugation (10 000 rpm, 10 min, 4 °C) before use. Cobalt protoporphyrin IX and reconstituted Mb with the cobalt complex were prepared according to the previous methods.[50,51] The solution of the purified Mb (100 mg/10 mL) was mixed with VC (10 mg) and the suspension was incubated for 4 h at 4 °C. The mixture was freeze-dried to prepare a catalyst precursor. About 100 mg of the ground powder on an alumina boat (length 80 mm, width 16 mm, height 10 mm) was placed in a quartz tube (diameter 50 mm, length 800 mm), which was then installed in a hinge split tube furnace (Koyo Thermo Systems Co. Ltd., KTF045N1). The samples were heated from ambient temperature to each of the target temperatures of 740, 840, 940, 1040 and 1140 °C for 1 h under N_2 flow (0.2 $L.min^{-1}$), and incubated for 2 h. The temperature of the sample inside the furnace was recorded with a thermocouple equipped with a data logger (CHINO MC3000). After cooling, the heat-treated catalysts were ground, and washed with 1 M HCl_{aq} and then with excess volumes of water twice. The dried catalysts were used for the experiments.

The catalyst sample (4.0 mg) was suspended in a 0.05 wt% Nafion solution in isopropanol (100 mL) and the catalyst ink was sonicated in an ultrasonic bath at 100 W at 35 kHz for 30 min. The ink (10 μL) was coated onto a glassy carbon electrode (GCE) with an area of 0.196 cm^2 and dried slowly at room temperature. Electrochemical measurements were carried out in a three-electrode cell connected to a potentiostat (ALS, electrochemical analyzer model 610B). A glassy carbon electrode (GCE) was used as the working electrode, Pt foil was employed as the counter electrode, and Ag/AgCl (+0.199 *vs.* SHE) was used as the reference electrode. Rotating disk electrode (RDE) experiments were performed in an O_2 or N_2 saturated 0.1 M $HClO_4$ solution at 25°C. Electrode rotation rates were controlled using a Pine Instruments AFMSRCE rotator with a Pine MSRX motor controller.

Physical measurements

X-ray diffraction (XRD) measurements were performed using a Rigaku SmartLab diffractometer with CuKα radiation. XRD patterns were recorded in the 2θ range from 5° to 60°. Raman spectra were obtained using a Jasco NRS-3100 spectrometer with an excitation wavelength of 532 nm. The powder sample was measured on the glass plates. X-ray photoelectron spectroscopy (XPS) measurements were performed with Shimadzu KRAROS AXIS−165x instrument using monochromatic Mg Kα radiation (1253.6 eV). The system was calibrated with a C1s peak at 284.5 eV. The samples were fixed as powder on a stainless steel sample holder with a double adhesive carbon tape. Transmission electron microscopy (TEM) measurements were performed using Hitachi HF-2000 with an acceleration voltage of 100 kV. The samples were prepared by adding 1.0 mg of the catalyst, Mb@VC prepared at 940 °C, into a solution, with subsequent ultrasonication for 5 min. The sample ink was loaded onto a 150-mesh molybdenum microgrid (Okenshoji Co., Ltd.), and the sample was dried at room temperature.

References and Notes

1. M. K. Debe, *Nature*, 2012, **486**, 43−51.
2. R. Jasinski, *Nature*, 1964, **201**, 1212-1213.
3. F. C. Anson, C. Shi and B. Steiger, *Acc. Chem. Res.*, 1997, **30**, 437–444.
4. H. Jahnke, M. Schönborn and G. Zimmermann, *Top. Curr. Chem.*, 1976, **61**, 133−181.
5. V. S. Bagotzky, M. R. Tarasevich, K. A. Radyushkina, O. A. Levina and S. I. Andrusyova, *J. Power Sources*, 1978, **2**, 233-240.
6. R. Holze, I. Vogel and W. Vielstich, *J. Electroanal. Chem.*, 1986, **210**, 277–286.
7. A. A. Tanaka, C. Fierro, D. Scherson and E. B. Yaeger, *J. Phys. Chem.*, 1987, **91**, 3799–3807.
8. J. A. R. van Veen, H. A. Colijn and J. F. van Baar, *Electrochimica Acta*, 1988, **33**, 801–804.
9. A. Widelöv and R. Larsson, *Electrochimica Acta*, 1992, **37**, 187–197.
10. A. Widelöv, *Electrochimica Acta*, 1993, **38**, 2493–2502.
11. G. Lalande, G. Faubert, R. Côté, D. Guay, J. P. Dodelet, L. T. Weng and P. Bertrand, *J. Power Sources*, 1996, **61**, 227–237.
12. A. L. Bouwkamp-Wijnoltz, W. Visscher and J. A. R. van Veen, *Electrochimica Acta*, 1998, **43**, 3141–3152.
13. S. L. Gojković, S. Gupta and R. F. Savinell, *J. Electroanal. Chem.*, 1999, **462**, 63–72.
14. M. Lefèvre, J. P. Dodelet and P. Bertrand, *J. Phys. Chem. B*, 2000, **104**, 11238–11247.
15. A. L. Bouwkamp-Wijnoltz, W. Visscher, J. A. R. van Veen, E. Boellaard, A. M. van der Kraan and S. C. Tang, *J. Phys. Chem. B*, 2002, **106**, 12993–13001.
16. M. Lefèvre and J.-P. Dodelet, *Electrochimica Acta*, 2003, **48**, 2749–2760.
17. H. Schulenburg, S. Stankov, V. Schünemann, J. Radnik, I. Dorbandt, S. Fiechter, P. Bogdanoff and H. Tributsch, *J. Phys. Chem. B*, 2003, **107**, 9034–9041.
18. R. Bashyam and P. Zelenay, *Nature*, 2006, **443**, 63−66.
19. M. Lefèvre, E. Proietti, F. Jaouen and J.-P. Dodelet, *Science*, 2009, **324**, 71−74.
20. G. Wu, K. L. More, C. M. Johnston and P. Zelenay, *Science*, 2011, **332**, 443−447.
21. H. T. Chung, J. H. Won and P. Zelenay, *Nat. Commun.*, 2013, **4**, 1922.
22. E. Proietti, F. Jaouen, M. Lefèvre, N. Larouche, J. Tian, J. Herranz and J.-P. Dodelet, *Nat. Commun.*, 2011, **2**, 416.
23. *Handbook of Metalloproteins*, Vol. 1, John Wiley &Sons, Ltd.: Chichester, 2001.
24. T. Tsukihara, H. Aoyama, E. Yamashita, T. Tomizaki, H. Yamaguchi, K. Shinzawa-Itoh, R. Nakashima, R. Yaono and S. Yoshikawa, *Science*, 1995, **269**, 1069–1074.
25. T. Tsukihara, H. Aoyama, E. Yamashita, T. Tomizaki, H. Yamaguchi, K. Shinzawa-Itoh, R. Nakashima, R. Yaono and S. Yoshikawa, *Science*, 1996, **272**, 1136−1144.
26. V. R. I. Kaila, M. I. Verkhovsky and M. Wikström, *Chem. Rev.*, 2010, **110**, 7062–7081.
27. J. P. Collman, R. Boulatov, C. J. Sunderland and L. Fu, *Chem. Rev.*, 2004, **104**, 561–588.

28. E. Kim, E. E. Chufán, K. Kamaraj and K. D. Karlin, *Chem. Rev.*, 2004, **104**, 1077–1134.
29. M. A. Thorseth, C. E. Tornow, E. C. M. Tse and A. A. Gewirth, *Coord. Chem. Rev.*, 2013, **257**, 130–139.
30. X. Liu, Y. Yu, C. Hu, W. Zhang, Y. Lu and J. Wang, *Angew. Chem. Int. Ed.*, 2012, **51**, 4312–4316.
31. S. Mukherjee, K. Sengupta, M. R. Das, S. S. Jana and A. Dey, *J. Biol. Inorg. Chem.*, 2012, **17**, 1009–1023.
32. S. Mukherjee, S. Bandyopadhyay, S. Chatterjee and A. Dey, *Chem. Commun.*, 2014, **50**, 12304–12307.
33. R. Jiang, D. T. Tran, J. P. McClure and D. Chu, *Electrochimica Acta*, 2012, **75**, 185–190.
34. J. B. Xu, T. S. Zhao and L. Zeng, *J. Hydrogen. Energy*, 2012, **37**, 15976–15982.
35. J. Maruyama and I. Abe, *Chem. Mater.*, 2005, **17**, 4660–4667.
36. J. Maruyama and I. Abe, *Chem. Mater.*, 2006, **18**, 1303−1311.
37. J. Maruyama, J. Okamura, K. Miyazaki, Y. Uchimoto and I. Abe, *J. Phys. Chem. C*, 2008, **112**, 2784–2790.
38. T. Hayashi, Y. Hitomi, T. Takimura, A. Tomokuni, T. Mizutani, Y. Hisaeda and H. Ogoshi, *Coord. Chem. Rev.*, 1999, **190-192**, 961–974.
39. H. Sato, M. Watanabe, Y. Hisaeda and T. Hayashi, *J. Am. Chem. Soc.*, 2005, **127**, 56–57.
40. T. Matsuo, A. Hayashi, M. Abe, T. Matsuda, Y. Hisaeda and T. Hayashi, *J. Am. Chem. Soc.*, 2009, **131**, 15124–15125.
41. A. Onoda, T. Himiyama, K. Ohkubo, S. Fukuzumi and T. Hayashi, *Chem. Commun.*, 2012, **48**, 8054–8056.
42. K. Oohora, Y. Kihira, E. Mizohata, T. Inoue and T. Hayashi, *J. Am. Chem. Soc.*, 2013, **135**, 17282–17285.
43. T. Hayashi, Y. Sano and A. Onoda, *Israel J. Chem.*, 2015, **55**, 76–84.
44. T. Jawhari, A. Roid and J. Casado, *Carbon*, 1995, **33**, 1561−1565.
45. Y. Wang, D. C. Alsmeyer and R. L. McCreery, *Chem. Mater.*, 1990, **2**, 557−563.
46. G. Faubert, R. Côté, J. P. Dodelet, M. Lefèvre and P. Bertrand, *Electrochimica Acta*, 1999, **44**, 2589–2603.
47. J. Casanovas, J. M. Ricart, J. Rubio, F. Illas and J. M. Jiménez-Mateos, *J. Am. Chem. Soc.*, 1996, **118**, 8071–8076.
48. J. R. Pels, F. Kapteijn, J. A. Moulijn, Q. Zhu and K. M. Thomas, *Carbon*, 1995, **33**, 1641−1653.
49. A. J. Bard and L. R. Faulkner, *Electrochemical Methods: Fundamentals and Applications, 2nd Edition; New York : John Wiley & Sons*, 2001.
50. T. Matsuo, T. Tsuruta, K. Maehara, H. Sato, Y. Hisaeda and T. Hayashi, *Inorg. Chem.*, 2005, **44**, 9391–9396.
51. T. Yonetani, H. Yamamoto and G. V. Woodrow, *J. Biol. Chem.*, 1974, **249**, 682–690.

Chapter 2

Nonprecious-metal Fe/N/C catalysts prepared from π-expanded Fe salen precursors toward an efficient oxygen reduction reaction

2-1. Introduction

Electrochemical reduction of O_2 is a key reaction for improving the performance of energy conversion devices such as fuel cells, metal-air batteries, and electrolyzers.[1-3] In particular, polymer electrolyte fuel cells (PEFCs) have been recognized as efficient energy converters enabling low emissions and low environmental impacts. Precious metal group (PMG) catalysts have been the most widely used catalysts for the cathodic oxygen reduction reaction (ORR) in PEFCs.[4–6] However, the high cost and low abundance of precious metals have been the main obstacles facing widespread commercialization of PEFCs. This situation has stimulated extensive investigations for development of alternative low-cost non-precious metal catalysts (NPMCs).[7–9] Carbon catalysts containing a first row transition metal, such as Fe or Co, and nitrogen (which are known as M/N/C catalysts), have been generally considered to represent promising alternatives to the PGM catalysts, because the M/N/C catalysts have been shown to promote high levels of ORR activity while having suitable durability for use in PEFCs.[10–15] Studies on M/N/C catalysts were initiated after the discovery of the ORR activity of cobalt phthalocyanine under alkaline conditions.[16] The pyrolyzed transition metal (Fe or Co) macrocycles adsorbed on carbon supports have been proven to improve ORR activity and stability under acidic conditions, which is a requirement for PEFCs.[17,18] A breakthrough study by Yeager revealed that the often-expensive macrocycles can be replaced with individual nitrogen and metal precursors.[19] Therefore, a series of low-cost nitrogen precursors such as phenanthroline,[10] polypyrrole,[11] and polyaniline[12] have been utilized in the preparation of M/N/C catalysts. The exact chemical structures of the metal-containing active sites in M/N/C catalysts prepared by pyrolysis is still under debate,[20,21] although a general $M{-}N_x$ site structure has been proposed on the basis of various

spectroscopic techniques.[22–24] It is believed that metals coordinated by the N-groups play an important role in enhancing the ORR activity of M/N/C catalysts.[10,25]

It has been demonstrated that the chemical structure of metal complex precursors is critical for the graphitization process that incorporates the metal and nitrogen atoms into carbon materials to form the M/N/C active sites. The optimization of nitrogen sources,[26] transition metal species,[27] and carbon supports,[7] has been investigated to control the M/N/C active sites and enhance the ORR activity. The auhtor began focusing on a new method by systematically tuning an aromatic framework of Fe complex precursors to improve the ORR activity of M/N/C catalysts. An Fe(Salen) complex is a low-cost precursor that enables simple diversification of the chemical structure of the N-containing ligands. He designed Fe(Salen) derivatives attached to various aromatic moieties, which are expected to have higher thermal stability to optimize the annulation process of the complexes during pyrolysis. In this work, he describe preparation and characterization of the Fe/N/C catalysts via pyrolysis of the π-expanded Fe(Salen) complexes (Fe(Xsal)) and their ORR activity. It is found that tuning the ligand structure of the Fe(Xsal) precursor leads to a remarkable positive shift (+50 mV) of onset potentials and an increase in efficiency of the four-electron reduction process in the ORR activity of pyrolyzed Fe/N/C catalysts.

2-2. Results and Discussion

Preparation of Fe/N/C catalysts

A series of precursors, Fe(Xsal) complexes with expanded aromatic ligand frameworks were synthesized according to the literature; Fe(Salen)Cl, Fe(saloph)Cl, *N*,*N*´-bis(1-hydroxy-2-naphthylidene)ethylene diaminoiron(III) chloride (Fe(1NAED)Cl), *N*,*N*´-bis(1-hydroxy-2-naphthylidene)-1,2-phenylenediaminoiron(III) chloride (Fe(1NAPD)Cl), *N*,*N*´-bis(2-hydroxy-1-naphthylidene)ethylenedi- aminoiron(III) chloride Fe(2NAED)Cl, and *N*,*N*´-bis(2-hydroxy-1-naphthylidene)-1,2-phenylenediaminoiron(III) chloride (Fe(2NAPD)Cl) (Figure 2-1a).[28–30] The thermal decomposition temperatures (T_D) values of Fe(1NAED)Cl, and Fe(2NAED)Cl with the expanded aromatic ring framework are shifted more than 30 °C above the T_D value of Fe(Salen)Cl. In addition, the T_D of Fe(Xsal) complexes with the *o*-phenylenediamine bridge (Fe(saloph)Cl, Fe(1NAPD)Cl, and Fe(2NAPD)Cl) range between 375 − 417 °C, which are approximately 40 °C higher relative to the Fe(Xsal) complexes with the ethylenediamine bridge (Fe(Salen)Cl, Fe(1NAED)Cl, and Fe(2NAED)Cl) (Figure 2-2). The thermogravimetric analysis of the precursor indicates that the aromatic rings in the ligand frameworks significantly enhance the thermal stability of Fe(Xsal) complexes during pyrolysis.

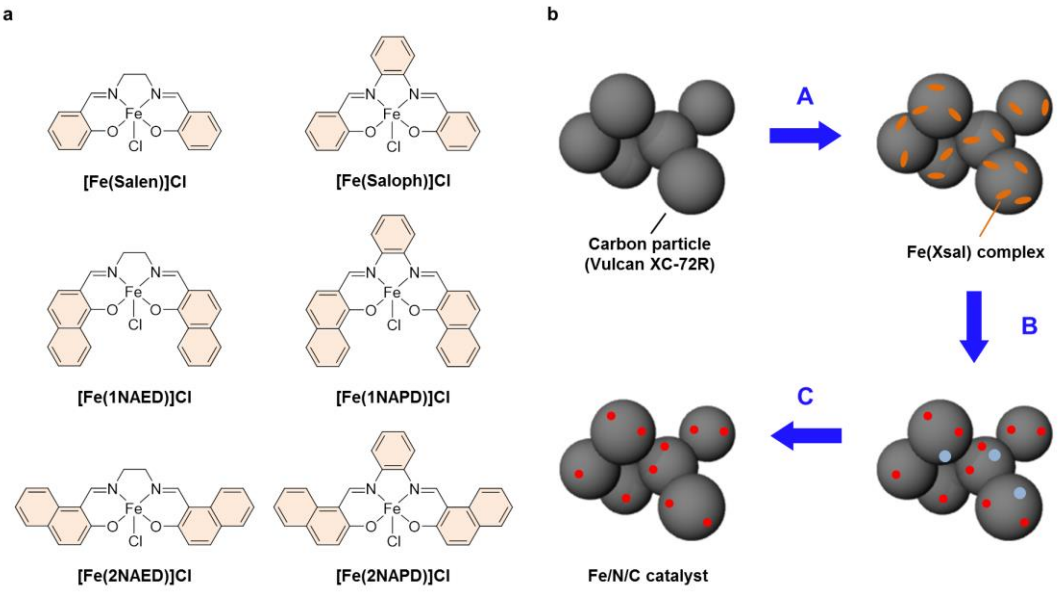

Figure 2-1. Structures of Fe(Xsal) complexes as precursors and the preparation of Fe/N/C catalysts. (a) Structures of Fe(Salen)Cl, Fe(Saloph)Cl, Fe(1NAED)Cl, Fe(1NAPD)Cl, Fe(2NAED)Cl, and Fe(2NAPD)Cl. (b) (A) The Fe(Xsal) complex (orange) is mixed with carbon materials, (B) pyrolyzed under N_2 atmosphere, and (C) treated with H_2SO_{4aq} to remove iron impurities (blue) and to prepare Fe/N/C catalysts containing the iron active sites (red).

The Fe/N/C electrocatalysts were prepared by pyrolysis of the mixture of the Fe(Xsal) complexes and carbon black (VC; Vulcan XC-72R, Cabot) (Figure 2-1b). The Fe(Xsal) complex dissolved in CH_2Cl_2 was vigorously mixed with VC and the solvent was removed to afford the precursor. The obtained precursor was preheated to 300 °C for 1 h and then incubated for 2 h under constant N_2 gas flow. The carbon materials were immediately pyrolyzed at 1000 °C for 2 h under constant N_2 gas flow for carbonization.[31] The pyrolyzed powder was ground and leached in an acidic solution (0.5 M H_2SO_4) to remove inactive species such as iron oxide and unincorporated iron species. After washing twice with an excess of water and drying, the Fe/N/C catalysts, Fe/Salen@VC, Fe/Saloph@VC, Fe/1NAED@VC, Fe/1NAPD@VC, Fe/2NAED@VC and Fe/2NAPD@VC, were used in further experiments.

Characterization of the Fe/N/C catalysts

The carbon materials in the Fe/N/C catalysts were first analyzed by Raman spectroscopy (Figure 2-3a). It is known that highly ordered graphite has a band between 1100 and 1700 cm^{-1}, whereas a disordered carbon structure has significantly different spectral characteristics with a D (disorder) band in the vicinity of 1355 cm^{-1}. In addition, graphitized carbons give rise to a G (graphite) band in the vicinity of 1580 cm^{-1}, which is assignable to in-plane displacement of the carbon strongly coupled in the hexagonal sheets.[32,33] The Raman spectra of the Fe/N/C catalysts presenting typical D- and G-bands indicate that the disordered

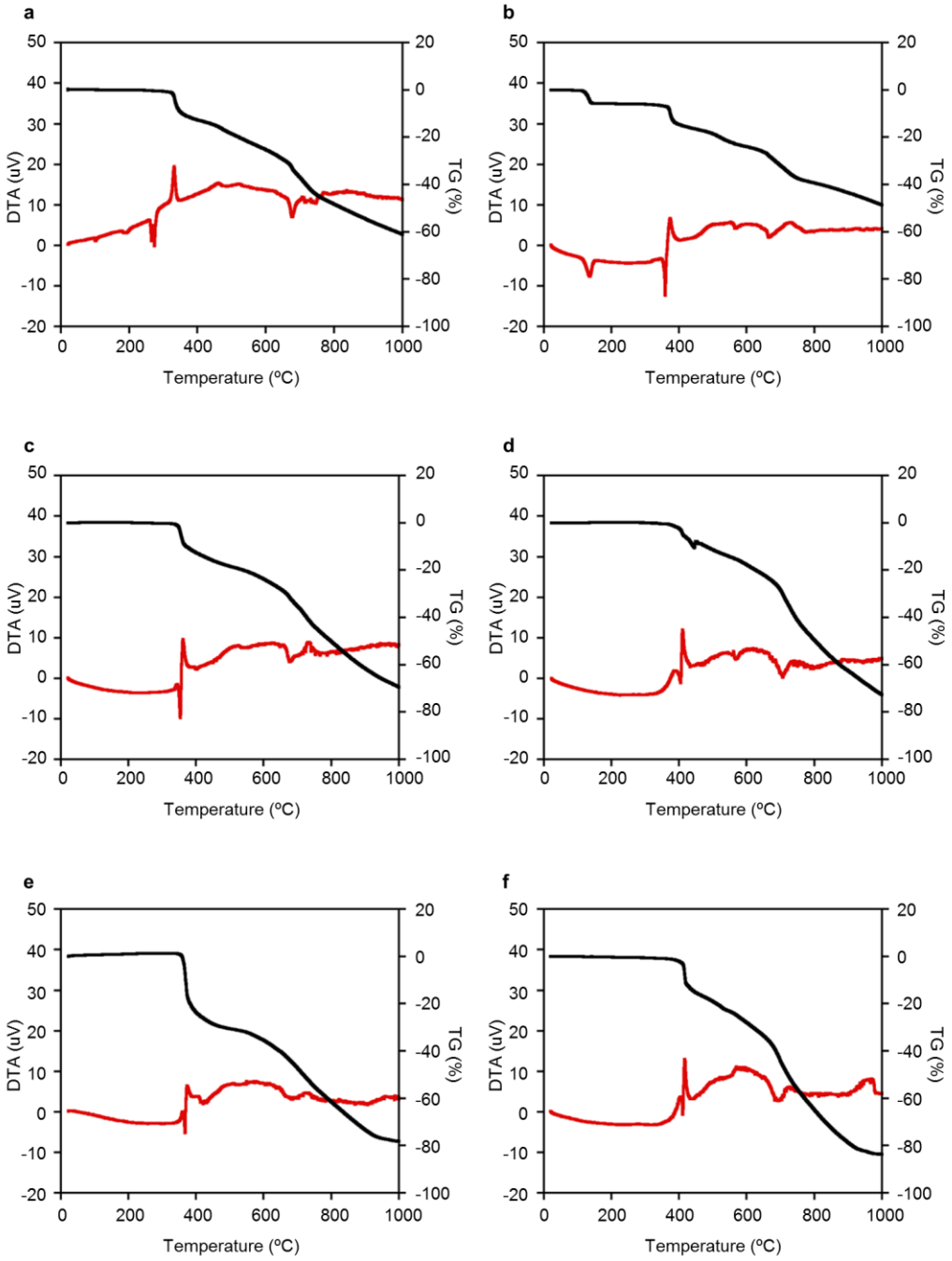

Figure 2-2. Thermogravimetric analysis curves (black) and differential thermal analysis curves (red) of Fe(Xsal) precursors. (a) Fe(salen)Cl, (b) Fe(saloph)Cl, (c) Fe(1NAED)Cl, (d) Fe(1NAPD)Cl, (e) Fe(2NAED)Cl, and (f) Fe(2NAPD).

carbonaceous structure is included in the Fe/N/C catalysts. The integrated intensity ratio I_D/I_G for the D-band and G-band is widely used to quantify the defects in graphitic materials. The I_D/I_G ratio for the six Fe/N/C catalysts is approximately 1.1, suggesting that all Fe/N/C catalysts contain similar content of graphitic and disordered structure in the carbonaceous materials. The nitrogen-doped graphene has been

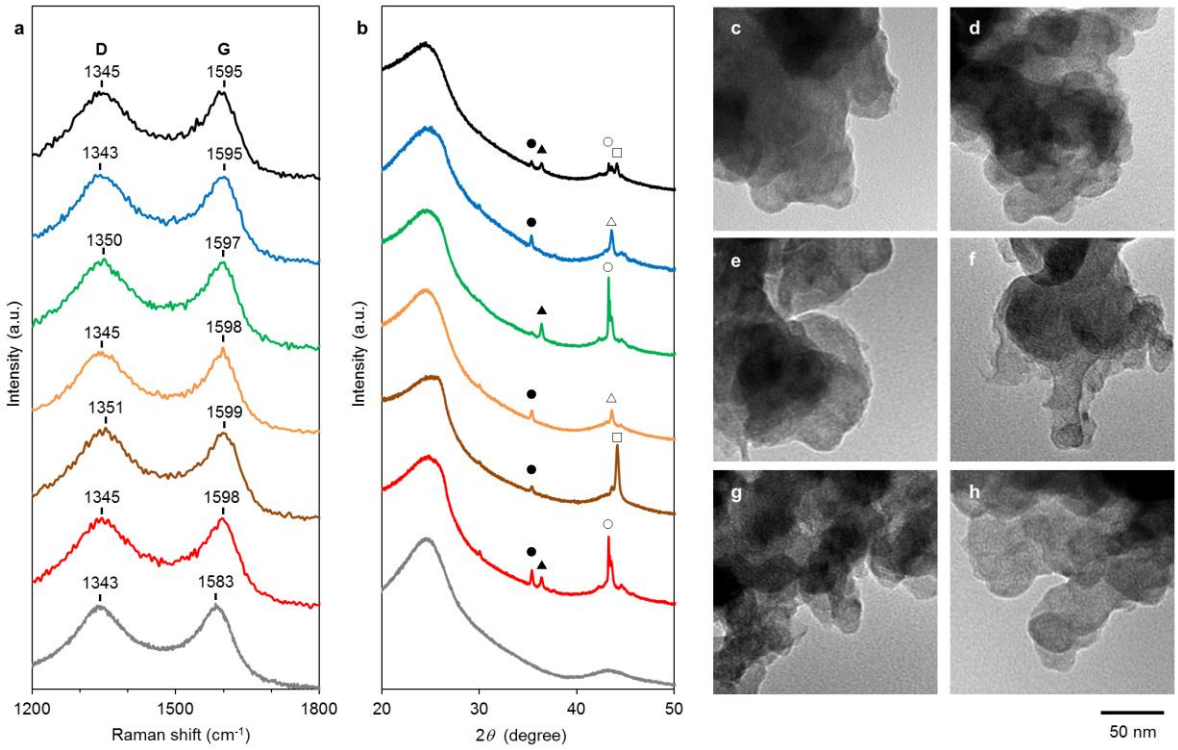

Figure 2-3. (a) Raman spectra and (b) XRD patterns of the Fe/N/C catalysts. Fe/Salen@VC (black), Fe/Saloph@VC (blue), Fe/1NAED@VC (green), Fe/1NAPD@VC (orange), Fe/2NAED@VC (brown), Fe/2NAPD@VC (red), and pyrolyzed VC (gray). The XRD peaks are assigned to Fe_3O_4 (JCPDS 00-001-1111) (closed circle), Fe_2O_3 (JCPDS 00-016-0895) (closed triangle), Fe_3C (JCPDS 01-089-3689) (open circle), Fe_3C (JCPDS 00-034-0001) (open triangle), and Fe_5C_2 (JCPDS 03-065-6169) (open square). TEM images of (c) Fe/Salen@VC, (d) Fe/Saloph@VC, (e) Fe/1NAED@VC, (f) Fe/1NAPD@VC, (g) Fe/2NAED@VC, and (h) Fe/2NAPD@VC.

known to show D' peak near 1600 cm^{-1}.[34–36] The G band peaks for the Fe/N/C catalysts exhibit near 1600 cm^{-1}, which shift from the peak at 1580 cm^{-1} for VC without nitrogen atom. This result indicates that nitrogen atoms are doped in the carbon materials. X-ray diffraction (XRD) patterns also confirm that each carbonaceous structure of the Fe/N/C catalysts prepared from the Fe(Xsal) complexes is very similar (Figure 2-3b). In general, powder samples of carbons in an amorphous structure provide diffraction peaks for (002) (2θ = *ca.* 26.0°), and (101) (2θ = *ca.* 44.0°).[37,38] The carbon catalysts were found to exhibit a strong and broad peak at ca. 26.0° and a weak and broad peak at 44.0°. The degree of graphitization of the Fe/N/C catalysts can be estimated on the basis of the relative intensities of reflections from the (002) and (101) planes according to the empirical formula. The degree of graphitization of the Fe/N/C catalysts (I_{002}/I_{101}: 3.9 for Fe/Salen@VC, 3.8 for Fe/Saloph@VC, 3.9 for Fe/1NAED@VC, 4.0 for Fe/1NAPD@VC, 3.5 for Fe/2NAED@VC, and 3.8 for Fe/2NAPD@VC) were determined from XRD. This also indicates that the carbonaceous structures of the Fe/N/C catalysts containing the iron active sites are similar. The

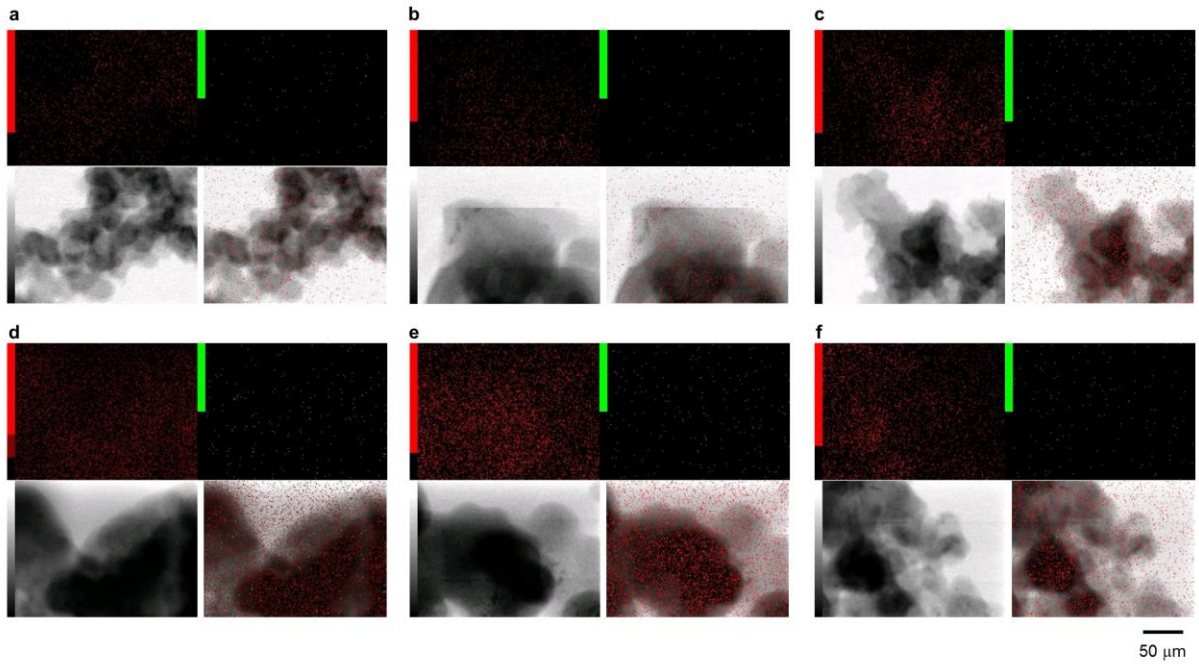

Figure 2-4. Physical characterization of the Element mapping images of carbon (upper left: red) and iron (upper right: green), TEM images (lower left), and overlaid TEM images (lower right) of Fe/N/C catalysts. (a) Fe/Salen@VC, (b) Fe/Saloph@VC, (c) Fe/1NAED@VC, (d) Fe/1NAPD@VC, (e) Fe/2NAED@VC, (f) Fe/2NAPD@VC.

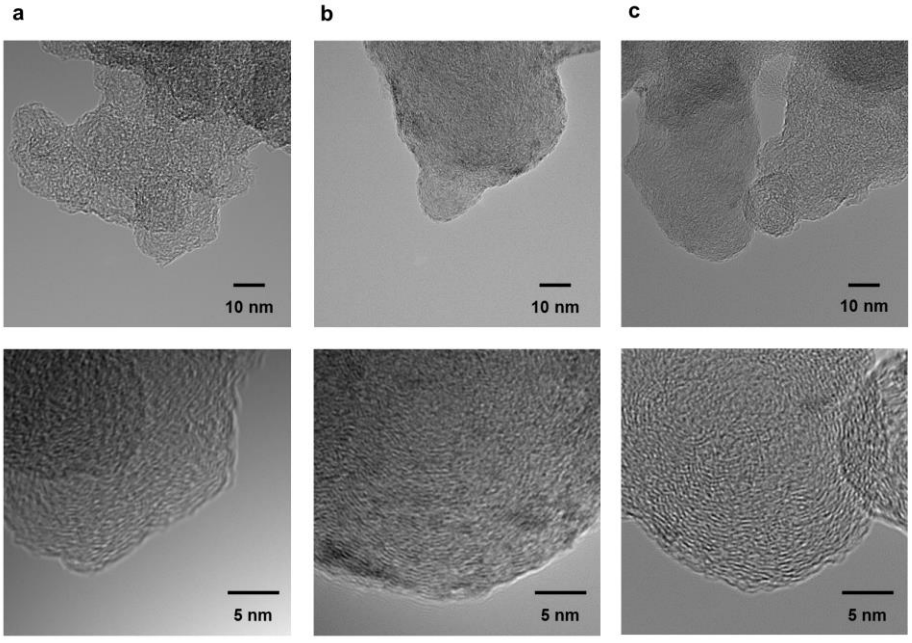

Figure 2-5. HRTEM images of (a) Fe/Salen@VC, (b) Fe/2NAPD@VC, and (c) Pyrolyzed VC. (magnification = 300k and 1000k). The iron contents of the samples determined by EDS analysis with an electron probe of 25 nm in the area with 300k magnification are (a) 0.69 wt%, (b) 0.79 wt%, and (c) 0.00 wt%.

peaks close to 44.0º indicate the presence of Fe_3C and Fe_5C_2 in the Fe/N/C catalysts (Figure 2-3b).[39,40] The peaks at 35.4° and 36.4° also indicate the presence of Fe_3O_4 and Fe_2O_3.[41,42] Judging from the values of reference intensity ratio (RIR) factor, I/I_{cor} (I_{cor}, integrated intensity of the corundum peak used for the RIR) ($I/I_{cor}(Fe_3O_4)$ = 141.3, $I/I_{cor}(Fe_3C)$ = 6.93, $I/I_{cor}(Fe_5C_2)$ = 1.98), the contents of Fe_3O_4 species are less than 1.8 % relative to that of the iron carbide species involved in the Fe/N/C catalysts.

Transmission electron microscope (TEM) images of the Fe/N/C catalysts with elemental mapping reveal that the iron species are well-dispersed within the carbon catalysts (Figures 2-3c–h, 2-4, and 2-5). The Fe/N/C catalysts have a spherical form with diameters ranging from 40 to 70 nm, which are retained in the structure of VC. Iron nanoparticles were not observed in TEM images, suggesting that Fe active sites are atomically dispersed within the carbon structure.

The content of N and Fe atoms in the Fe/N/C catalysts was determined by elemental analysis with inductively coupled plasma atomic emission spectrometry (ICP-AES) measurements. The elemental compositions of the Fe/N/C catalysts prepared from Fe(Xsal) precursors with different ligand frameworks are summarized in Table 1. Although each carbonaceous structure in the series of Fe/N/C catalysts is very similar, the N and Fe content of each of Fe/Saloph@VC, Fe/1NAPD@VC and Fe/2NAPD@VC (which were prepared from phenylene-bridged precursors) is higher than the N and Fe content of ethylene-bridged precursors. These results suggest that the aromatic rings in the Xsal ligand frameworks enhance incorporation of N and Fe atoms into carbon materials during pyrolysis, thereby increasing the content of both N and Fe in the Fe/N/C catalysts.

ORR activity

The ORR activities of the Fe/N/C catalysts were determined on a rotating disk electrode (RDE) (Figure 2-6a). The measurements were performed using RDE rotated at 2000 rpm in a medium of O_2 saturated 0.1 M $HClO_4$ at pH 1. All Fe/N/C catalysts prepared from the Fe(Xsal) precursors show significant cathodic current during O_2 reduction, indicating high levels of ORR activity. The onset potential of O_2 reduction with the Fe/N/C catalysts shift positively when an Fe(Xsal) complex with the π-expanded ligand is used as a precursor. In particular, Fe/2NAED@VC (0.81 V) and Fe/2NAPD@VC (0.82 V) have significantly shifted onset potentials, suggesting that the introduction of aromatic rings to the ligand framework of the precursor positively shifts the onset potential by 50 mV in Fe/2NAPD@VC relative to Fe/Salen@VC (0.77 V). Furthermore, these findings demonstrate that the ORR catalyst obtained from the Fe(Xsal) precursor with the higher thermal stability promotes excellent ORR activity. The average number of electrons transferred during O_2 reduction (n) was calculated from Koutecky-Levich plots with ORR polarization

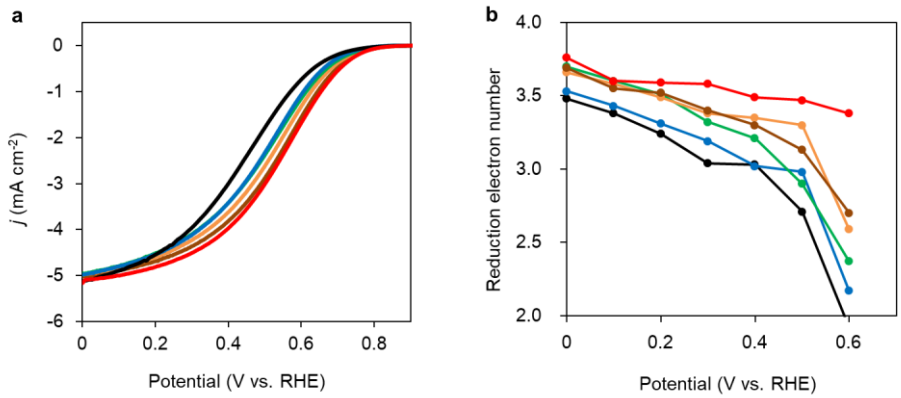

Figure 2-6. (a) ORR polarization curves in O_2-saturated 0.1 M $HClO_4$ solution at 5 $mV \cdot s^{-1}$ with 2000 rpm, and (b) the number of electrons transferred during O_2 reduction of Fe/N/C catalysts. Fe/Salen@VC (black), Fe/Saloph@VC (blue), Fe/1NAED@VC (green), Fe/1NAPD@VC (orange), Fe/2NAED@VC (brown) and Fe/2NAPD@VC (red).

curves in a 0.1 M $HClO_4$ solution for each carbon catalyst (Figure 2-6b). The *n* value is 3.6 for Fe/2NAPD@VC, generally indicating occurrence of four electron reduction. Furthermore, this value is higher than that of Fe/Salen@VC (3.0). These results indicate that the carbon catalysts prepared from the Fe(Xsal) complexes promote four-electron reduction of O_2.

XANES and FT-EXAFS measurements

The structures of the iron species highly-dispersed in the carbon catalysts were further analyzed by X-ray absorption fine structure (XAFS) measurements. Fe K-edge X-ray absorption near-edge spectroscopy (XANES) was employed to determine the chemical state of the iron atoms in the catalysts (Figure 2-7a). The XANES spectra of FeO, Fe_2O_3, Fe-foil, and Fe_3C[42,43] were compared as standard samples (Figure 2-7b). The pre-edge and edge features of the carbon catalysts are clearly different from those of FeO, Fe_2O_3, and Fe-foil, whereas they match well with those of Fe_3C. In addition, the shape of the white line in the XANES spectrum of each of the Fe/N/C catalysts is similar to that of Fe_3C. This implies that the majority of the iron species among the Fe/N/C catalysts has electronic and chemical properties similar to those of Fe_3C. Next, to evaluate the environment of the iron atoms in the Fe/N/C catalysts, FT-EXAFS analysis was carried out as shown in Figure 2-7c. The Fe−Fe bond distances in Fe_3C, which is one of the candidates of the main component for the iron species, are known to be ca. 2.5−2.7 Å in the first coordination shell and ca. 4.0 Å in the second coordination shell.[39,42] In contrast, the Fe/N/C catalysts provide a sharply different profile as shown in Figure 2-7c. The presence of a strong peak near 2.1 Å and the absence of peaks near 4.0 Å provide support for this proposal that the iron atoms are located in the first coordination shell and that formation of general Fe_3C should be ruled out. This is consistent with the TEM results that show the

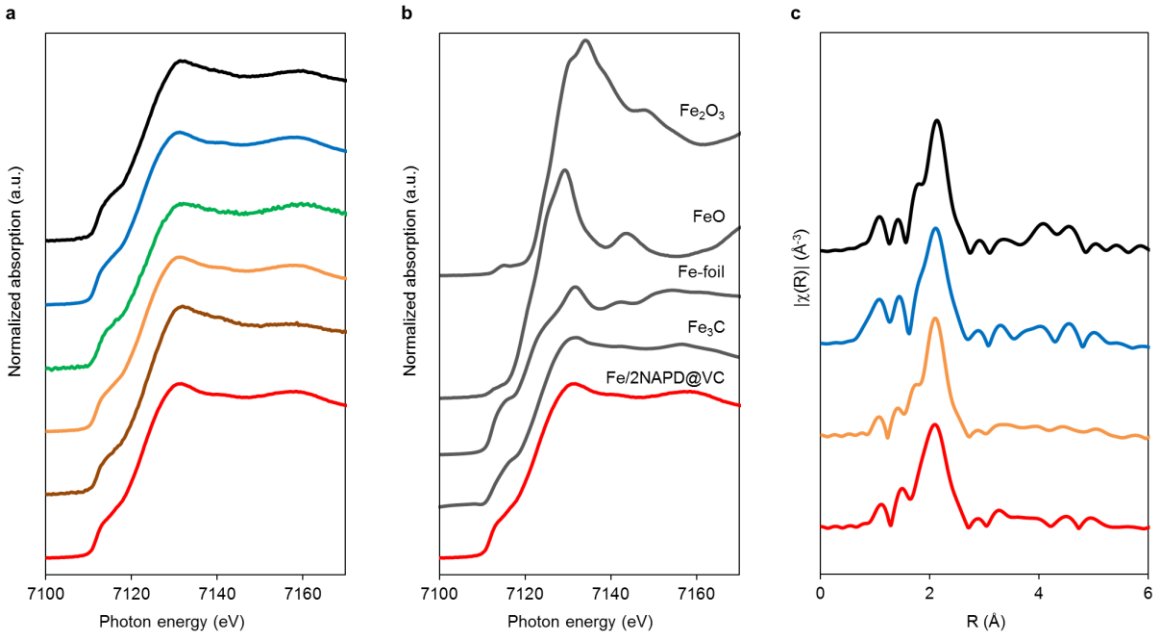

Figure 2-7. (a) Normalized XANES spectra of Fe/N/C catalysts: Fe/Salen@VC (black), Fe/Saloph@VC (blue), Fe/1NAED@VC (green), Fe/1NAPD@VC (orange), Fe/2NAED@VC (brown) and Fe/2NAPD@VC (red). (b) Normalized XANES spectra of reference samples, Fe_2O_3, FeO, Fe-foil, Fe_3C and Fe/2NAPD@VC (red). (c) FT-EXAFS of Fe/N/C catalysts: Fe/Salen@VC (black), Fe/Saloph@VC (blue), Fe/1NAPD@VC (orange), and Fe/2NAPD@VC (red).

absence of clear iron particles within the nanometer size range. A weak peak near 4.0 Å is found in the case of Fe/Salen@VC. In contrast, Fe/N/C catalysts prepared from Fe(Xsal) precursors do not show the peak. Furthremore, the small peak identified in the range below 2.1 Å should be assigned to Fe−C and N bonds connecting the iron sites and the nitrogen-containing carbon support.[44–46] The peak intensity of this region is greater for Fe/1NAPD@VC and Fe/2NAPD@VC relative to that for Fe/Salen@VC. The EXAFS result indicates that the π-expanded structure of the precursor results in higher dispersion of the iron sites and the formation of $Fe-N_x$ structure.

XPS measurement

The chemical structures of the nitrogen atoms in the Fe/N/C catalyst were determined by X-ray photoelectron spectroscopy (XPS) measurements (Figure 2-8a). Four types of nitrogen species are confirmed by the N1s peaks in the range between 398.0 and 404.0 eV.[47,48] The N1s spectra were deconvoluted into four different nitrogen species including pyridinic N (398.0–398.9 eV), pyrrolic N (399.5−400.4 eV), graphitic N (400.5−402.0 eV), and *N*-oxide groups (N^+–O^-) at binding energies higher than 402.0 eV. Interestingly, the content of pyridinic N of the catalyst prepared from the Fe(Xsal) precursor

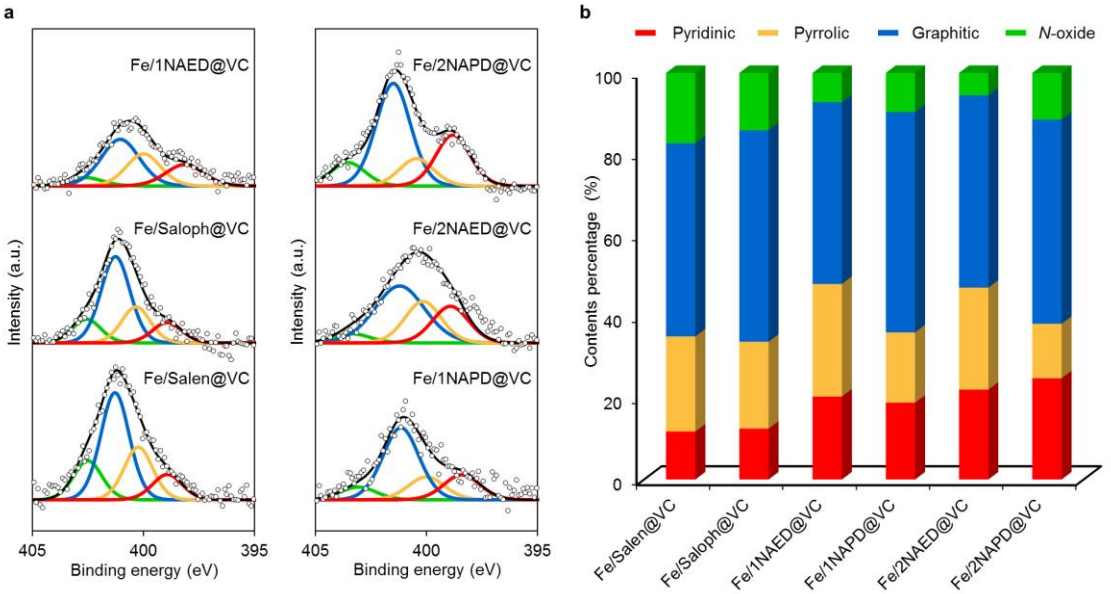

Figure 2-8. The distribution of pyridinic N, pyrrolic N, graphitic N and *N*-oxide in Fe/N/C catalysts. (a) XPS spectra of Fe/N/C catalysts in the N1s region with fitted peaks of pyridinic-N (red), pyrrolic-N (yellow), graphitic-N (blue) and *N*-oxide (green). (b) The proportion of four nitrogen species in the Fe/N/C catalysts.

Table 1. Characterization and electrochemical activity of Fe/N/C catalysts.

Fe/N/C catalyst[a]	T_D (°C)[a]	Elemental analysis		XPS (N1s)				E_{onset} (V)[c]	n[d]
		Fe[b] (wt%)	N (wt%)	Pyridinic (%)	Pyrrolic (%)	Graphitic (%)	*N*-oxide (%)		
Fe/Salen@VC	333	0.7	0.5	11.8	23.4	47.5	17.4	0.77	3.0
Fe/Saloph@VC	375	1.3	0.8	12.5	21.4	52.0	14.1	0.79	3.2
Fe/1NAED@VC	362	0.6	0.5	20.4	27.7	44.7	7.2	0.79	3.3
Fe/1NAPD@VC	411	1.0	0.8	18.9	17.3	54.2	9.6	0.80	3.4
Fe/2NAED@VC	375	0.4	0.6	22.1	25.1	47.3	5.5	0.81	3.4
Fe/2NAPD@VC	417	0.9	0.8	24.9	13.4	50.2	11.5	0.82	3.6

[a] Decomposition temperature of Fe(Xsal) precursors determined by TG-DTA. [b] Determined by ICP-AES. [c] The potential at I = 0.05 mA·cm^{-2} in RDE. [d] The number of electrons transferred during O_2 reduction at 0.3 V calculated by Koutecky-levich plots.

with the expanded aromatic rings is increased: 11.8% for Fe/Salen@VC, 12.5% for Fe/Saloph@VC, 20.4% for Fe/1NAED@VC, 18.9% for Fe/1NAPD@VC, 22.1% for Fe/2NAED@VC, and 24.9% for Fe/2NAPD@VC, although the proportions of the other nitrogen species vary for each of Fe/N/C catalysts prepared from different precursors (Figure 2-8b). Taken together, these results indicate that higher content of pyridinic N provides higher ORR activity (Table 1). Therefore, the ligand frameworks of the precursors remarkably affect the content of pyridinic N in the Fe/N/C catalysts.

2-3. Conclusions

This work demonstrates a new method for improving the ORR activity of Fe/N/C catalysts by introducing aromatic moieties into the structures of Fe(Xsal) precursors. The Fe/N/C catalysts were prepared by pyrolysis of the mixture of carbon support and the Fe(Xsal) precursors. The catalysts prepared using the Fe(Xsal) complexes with π-expanded ligand frameworks such as the Fe(2NAPD) complex exhibit a remarkable positive shift (+ 50 mV) in the onset potential for ORR relative to catalysts prepared from the simple Fe(Salen) complex. XRD and XAFS analyses clarify that the main species of Fe exist as iron carbide in the Fe/N/C catalysts. As Fe nanoparticles were not observed in TEM images with elemental mapping, the iron species are dispersed within the carbonaceous structure in these catalysts. In particular, the Fe/N/C catalysts prepared from π-expanded Fe(Salen) complexes have iron species with an atomically dispersed structures as indicated by the EXAFS results. Furthermore, we clarified that the thermal stability of the ligand structures of the precursors increases the content of pyridinic nitrogen which forms the $Fe{-}N_x$ structure, resulting in improvement of the ORR activity although the initial structure of the Fe(Salen) complexes is not retained after pyrolysis. These findings prove that rational design of aromatic ligand frameworks for metal precursor complexes contributes to enhancement of ORR activity of non-precious M/N/C catalysts which are appropriate for incorporation into fuel cells and metal-air battery applications.

2-4. Experimental Section

Materials

All reagents were used without purification. All solvents were dried with molecular sieves 3A before use.

Synthesis of H_2(Xsal) ligands

The Schiff base ligands H_2(Xsal) were synthesized from the diamine (ethylenediamine or *o*-phenylenediamine) and salicylaldehyde (salicylaldehyde, 1-hydroxy-2-naphthaldehyde or 2-hydroxy-1-naphthaldehyde) in 1:2 molar ratio in dry methanol. The reaction mixture was refluxed for 1 h and cooled to room temperature. The yellow-orange precipitates were collected by filtration, washed with cool methanol, and dried to yield the product.

H_2(1NAED) [N,N´-bis(1-hydroxy-2-naphthalidene)-1,2-ethylenediamine]. Yield: 92%; color: yellow; ^{1}H NMR (400 MHz, DMSO-d_6) δ 13.04 (2H, s, OH), 8.25 (4H, m, N=C*H*, 8-*H*), 7.60 (2H, d, *J* = 8.0 Hz,

5-*H*), 7.54 (2H, t, *J* = 6.8 Hz, 8.0 Hz, 6-*H*), 7.37 (2H, t, *J* = 6.8 Hz, 8.0 Hz, 7-*H*), 7.01 (2H, d, *J* = 8.8 Hz, 3-*H*), 6.69 (2H, d, *J* = 8.8 Hz, 4-*H*), 3.91 (4H, s, C*H*$_2$).

H$_2$(1NAPD) [N,N´-bis(1-hydroxy-2-naphthalidene)-1,2-phenylenediamine]. Yield: 96%; color: orange; ^{1}H NMR (400 MHz, DMSO-d_6) δ 14.19 (2H, s, OH), 9.07 (2H, s, N=C*H*), 8.33 (2H, d, *J* = 8.0 Hz, 8-*H*), 7.80 (2H, d, *J* = 8.0 Hz, 5-*H*), 7.73–7.71 (2H, m, *J* = 6.0 Hz,, 3´-*H*), 7.64 (2H, t, *J* = 7.2 Hz, 8.0 Hz, 6-*H*), 7.59 (2H, d, *J* = 8.8 Hz, 3-*H*), 7.51 (2H, t, *J* = 7.2 Hz, 8.0 Hz, 7-*H*), 7.43–7.41 (2H, m, *J* = 6.0 Hz, 4´-*H*), 7.20 (2H, d, *J* = 8.8 Hz, 4-*H*).

H$_2$(2NAED) [N,N´-bis(2-hydroxy-1-naphthalidene)-1,2-ethylenediamine]. Yield: 95%; color: yellow; ^{1}H NMR (400 MHz, DMSO-d_6) δ 14.14 (2H, s, OH), 9.17 (2H, s, N=C*H*), 8.03 (2H, d, *J* = 7.2 Hz, 8-*H*), 7.72 (2H, dd, *J* = 9.6 Hz, 4-*H*), 7.63 (2H, d, *J* = 8.0 Hz, 5-*H*), 7.41 (2H, t, *J* = 7.2 Hz, 8.0 Hz, 7-*H*), 7.20 (2H, t, *J* = 8.0 Hz, 8.0 Hz, 6-*H*), 6.73 (2H, d, *J* = 9.6 Hz, 3-*H*), 4.02 (4H, s, C*H*2).

H$_2$(2NAPD) [N,N´-bis(2-hydroxy-1-naphthalidene)-1,2-phenylenediamine]. Yield: 54%; color: orange; ^{1}H NMR (400 MHz, DMSO-d_6) δ 15.12 (2H, s, OH), 9.70 (2H, s, N=C*H*), 8.54 (2H, d, *J* = 8.4 Hz, 8-*H*), 7.96 (2H, d, *J* = 9.2 Hz, 4-*H*), 7.84–7.81 (4H, m, 3´-*H*, 5-*H*), 7.55 (2H, t, *J* = 7.2 Hz, 8.4 Hz, 7-*H*), 7.46–7.43 (2H, m, *J* = 6.0 Hz, 4´-*H*), 7.37 (2H, t, *J* = 7.2 Hz, 8.0 Hz, 6-*H*), 7.06 (2H, d, *J* = 9.2 Hz, 3-*H*).

Synthesis of Fe(Xsal) complexes

Iron ion was inserted to H_2(Xsal) ligands by mixing $FeCl_3$ (1 equiv) in 300 mL of ethanol/acetone (1/1, v/v). The reaction mixture was refluxed for 2 h, and cooled to room temperature. The precipitates were collected by filtration, washed with a small portion of dried ethanol, and dried to yield the product.

[Fe(salen)Cl]. Yield: 54%; UV-vis (DMSO, nm): 302, 319, 483; ESI-TOF MS (positive mode): *m/z* = 322.03 (M^+), calcd for $C_{16}H_{14}FeN_2O_2$, 322.04.

[Fe(saloph)Cl]. Yield: 14%; UV-vis (DMSO, nm): 300, 375; ESI-TOF MS (positive mode): *m/z* = 370.03 [M^+], calcd for $C_{20}H_{14}FeN_2O_2$, 370.04.

[Fe(1NAED)Cl]. Yield: 53%; UV-vis (DMSO, nm):277, 315, 369; ESI-TOF MS (positive mode): *m/z* = 422.07 [M^+], calcd for $C_{24}H_{18}FeN_2O_2$, 422.07.

[Fe(1NAPD)Cl]. Yield: 37%; UV-vis (DMSO, nm): 301, 408; ESI-TOF MS (positive mode): *m/z* = 470.07 [M^+], calcd for $C_{28}H_{18}FeN_2O_2$, 470.07.

[Fe(2NAED)Cl]: Yield: 47%; UV-vis (DMSO, nm): 296, 309, 516; ESI-TOF MS (positive mode) *m/z* = 422.07 [M^+], calcd for $C_{24}H_{18}FeN_2O_2$, 422.07.

[Fe(2NAPD)Cl]: Yield: 69%; UV-vis (DMSO, nm): 334, 397, 453; ESI-TOF MS (positive mode) *m/z* = 470.07 [M^+], calcd for $C_{28}H_{18}FeN_2O_2$, 470.07.

Catalyst preparation

Carbon black Vulcan XC-72R (VC, Cabot, USA) was used as a carbon support. Electrocatalysts were prepared from Fe(Xsal) complexes and VC using a pyrolysis in N_2 gas flow. The electrocatalyst, which abbreviated to Fe/Xsal@VC, was prepared as follows: Fe(salen)Cl (30 mg, 84 μmol) was dissolved in a minimum volume of CH_2Cl_2 and mixed with a powder of VC (30 mg). The suspension was vigorously vortexed and sonicated for 30 min. The solvent was removed and residue was used as a precursor for an electrocatalyst. The precursor was placed on an alumina boat (length: 80 mm, width: 16 mm, height: 10 mm) which was then placed in a quartz tube (diameter 50 mm, length 800 mm). The quartz tube was installed in a hinge split tube furnace (Koyo Thermo Systems Co. Ltd., KTF045N1). The precursor was preheated from ambient temperature to 300 ℃ for 1 h under N_2 flow (0.2 $L \cdot min^{-1}$), and incubated for 2 h. The precursor was then heated to 1000 ℃ for 1 h immediately, and incubated for 2 h. The temperature of the sample inside the furnace was recorded with a thermocouple equipped with a data logger (CHINO Corporation, MC3000). After cooling, the pyrolyzed catalyst was ground and further treated in a 0.5 M H_2SO_4 solution at 80 ℃ for 3 h to leach out impurities such as iron oxide, and then washed with excess volumes of deionized water twice. The dried carbon catalyst was used for the experiments. Other carbon catalysts (Fe/Saloph@VC, Fe/1NAED@VC, Fe/1NAPD@VC, Fe/2NAED@VC and Fe/2NAPD@VC) were obtained using the same protocol with each indicated iron complex.

Physicochemical characterization

The decomposition temperatures of Fe(Xsal) complexes were determined by themogravimetry-differential thermal analysis (TG-DTA) using a Mac Science TG-DTA TMA DSC with a heating rate of 10 ℃ min^{-1} in an N_2 stream and platinum pan. Fe content of each of the Fe/N/C catalysts was characterized by inductively coupled plasma atomic emission spectroscopy (ICP-AES) using a SHIMAZDU ICPS-7510 system. Specific surface areas were obtained using a MicrotracBEL BELSORP-mini II system. The Raman spectra were obtained using a JASCO NRS-3100 instrument with a 532 nm laser. X-ray diffraction (XRD) patterns of the samples were obtained using an X-ray diffractometer (Rigaku, SmartLab) equipped with a Cu Kβ source. The contents of iron oxide for the catalysts were estimated by the peak intensity with the correction using the values of reference intensity ratio (RIR); 0.9% (Fe/Salen@VC), 1.3% (Fe/Saloph@VC), 1.8% (Fe/1NAPD@VC), 1.1% (Fe/2NAED@VC), and 1.2% (Fe/2NAPD@VC). Transmission electron microscopy (TEM) images were obtained using a HITACHI H-7650 microscope operated at 100 kV of accelerating voltage. High-resolution transmission electron microscopy (HRTEM) observations and the chemical composition analyses were carried out using a

HITACHI HF-2000 field emission TEM operated at an accelerating voltage of 200 kV. The chemical composition of each samples was analyzed by EDS made of NORAN Instruments. The analyses were carried out using an electron probe of approximately 25 nm in diameter. The characteristic X-ray of iron was collected with an ultra-thin window X-ray detector at a high take-off angle of 68 degrees. X-ray absorption spectroscopy (XAS) was performed at the BL11 beamline of SAGA Light Source (SAGA-LS) in Kyusyu, Japan. The Fe K-edge spectra were analyzed by Athena program.[49] X-ray photoelectron spectroscopy (XPS) measurements were performed on a KRATOS AXIS-165x (SHIMADZU) system, equipped with a Mg Kα X-ray source. Individual chemical components of the N 1s binding energy region were fitted to the spectra after a Tougaard-type background subtraction.

Electrochemical measurement.

A rotating disk electrode (RDE) with a glassy carbon disk electrode (ϕ =5 mm) was used for evaluation of the carbon catalysts. Electrode rotation rates were controlled using a Pine Instruments AFMSRCE rotator with a Pine MSRX motor controller. The electrode was polished to mirror flat with alumina powder (50 nm) before use. The catalyst ink included a mixture of 12.0 mg of catalyst (Fe/Salen@VC, Fe/Saloph@VC, Fe/1NAED@VC, Fe/1NAPD@VC, Fe/2NAED@VC or Fe/2NAPD@VC), and 50 μL of 5 wt% Nafion® solution (Sigma-Aldrich), and 950 μL of isopropanol. The ink was vortexed and sonicated in an ultrasonic bath at 100 W at 35 kHz for 30 min. Then 10 μL of catalyst ink was loaded onto the surface of the electrode and dried.

Electrochemical tests were carried out on a potentiostat (ALS, electrochemical analyzer model 610B) using a typical three-electrode system, with platinum wire as the counter electrode and Ag/AgCl as the reference electrode. The potential difference between Ag/AgCl and RHE was calculated and the value is 0.258 V in a 0.1 M $HClO_4$ solution. The scan rate for all measurements was 5 $mV \cdot s^{-1}$ from −0.258 to 0.742 V versus the Ag/AgCl reference electrode. Before each potential scan, the electrolyte of the 0.1 M $HClO_4$ solution was saturated with O_2 for at least 30 min, and O_2 purging was continued during the electrochemical experiments. The measured current was subtracted from the background current at the N_2-saturated electrolyte. The number of electrons transferred during O_2 reduction was calculated using the Koutecky–Levich equation (Equations. 2-1 and 2-2)[54]

$$I^{-1} = I_K^{-1} + I_L^{-1} \qquad (2\text{-}1)$$

$$I_L = 0.620nFAD_0^{2/3}\omega^{1/2}\nu^{-1/6}C_0 \qquad (2\text{-}2)$$

where I, I_K, and I_L represent the measured, kinetically-controlled, and diffusion-limited currents,

respectively. n is the number of exchanged electrons, ω is the angular frequency of rotation, $\omega = 2\pi f/60$, f is the RDE rotation rate in rpm, F is the Faraday constant (96,485 $C \cdot mol^{-1}$), D_0 is the diffusion coefficient of O_2 in 0.1 M $HClO_4$ solution (1.9 x 10^{-5} $cm^2 \cdot s^{-1}$), ν is the kinematic viscosity of electrolyte (9.87 x 10^{-3} $cm^2 \cdot s^{-1}$), and C_0 is the concentration of O_2 (11.8 x 10^{-6} $mol \cdot cm^{-3}$).

References and Notes

1. M. K. Debe, *Nature*, 2012, **486**, 43−51.
2. Q. Li, R. Cao, J. Cho and G. Wu, *Adv. Energy Mater.*, 2014, **4**, 1301415.
3. D. Higgins, P. Zamani, A. Yu and Z. Chen, *Energy Environ. Sci.*, 2016, **9**, 357−390.
4. J. Snyder, T. Fujita and M. W. Chen, J. Erlebacher, *Nat. Mater.*, 2010, **9**, 904−907.
5. A. Rabis, P. Rodriguez and T. J. Schmidt, *ACS Catal.*, 2012, **2**, 864−890.
6. M. Shao, Q. Chang, J.-P. Dodelet and R. Chenitz, *Chem. Rev.*, 2016, **116**, 3594−3657.
7. F. Jaouen, E. Proietti, M. Lefevre, R. Chenitz, J.-P. Dodelet, G. Wu, H. T. Chung, C. M. Johnston and P.Zelenay, *Energy Environ. Sci.*, 2011, **4**, 114−130.
8. Z. Chen, D. Higgins, A. Yu, L. Zhang and J. Zhang, *Energy Environ. Sci.*, 2011, *4*, 3167−3192.
9. G. Wu and P. Zelenay, *Acc. Chem. Res.*, 2013, **46**, 1878−1889.
10. R. Bashyam and P. Zelenay, *Nature*, 2006, **443**, 63−66.
11. M. Lefèvre, E. Proietti, F. Jaouen and J.-P. Dodelet, *Science*, 2009, **324**, 71−74.
12. G. Wu, K. L. More, C. M. Johnston and P. Zelenay, *Science*, 2011, **332**, 443−47.
13. Y. Liang, Y. Li, H. Wang, J. Zhou, J. Wang, T. Regier and H. Dai, *Nat. Mater.*, 2011, **10**, 780−786.
14. Y. Nabae, M. Sonoda, C. Yamauchi, Y. Hosaka, A. Isoda and T. Aoki, *Catal. Sci. Tech.*, 2014, **4**, 1400−1406.
15. T. Ishii, T. Maie, M. Hamano, T. Kishimoto, M. Mizushiri, Y. Imashiro and J.-i. Ozaki, *Carbon*, 2017, **116**, 591−598.
16. R. Jasinski, *Nature*, 1964, **201**, 1212−1213.
17. H. Jahnke, M. Schönborn and G. Zimmermann, *Top. Curr. Chem.*, 1976, **61**, 133−181.
18. G. Lalande, R. Côté, G. Tamizhmani, D. Guay, J. P. Dodelet, L. Dignard-Bailey, L. T. Weng and P. Bertrand, *Electrochim. Acta*, 1995, **40**, 2635-−2646.
19. S. Gupta, D. Tryk, I. Bae, W. Aldred and E. Yeager, *J. Appl. Electrochem.*, 1989, **19**, 19−27.
20. J.-P. Dodelet, R. Chenitz, L. Yang and M. Lefèvre, *ChemCatChem*, 2014, **6**, 1866−1867.
21. Y. Hu, J. O. Jensen, W. Zhang, L. N. Cleemann, W. Xing, N. J. Bjerrum and Q. Li, *Angew. Chem. Int. Ed.*, 2014, **53**, 3675−3679.
22. U. I. Kramm, J. Herranz, N. Larouche, T. M. Arruda, M. Lefevre, F. Jaouen, P. Bogdanoff, S. Fiechter, I. Abs-Wurmbach, S. Mukerjee and J.-P. Dodelet, *Phys. Chem. Chem. Phys.*, 2012, **14**, 11673−11688.
23. N. Ramaswamy, U. Tylus, Q. Jia and S. Mukerjee, *J. Am. Chem. Soc.*, 2013, **135**, 15443−15449.
24. Q. Jia, N. Ramaswamy, U. Tylus, K. Strickland, J. Li, A. Serov, K. Artyushkova, P. Atanassov, J. Anibal, C. Gumeci, S. C. Barton, M.-T. Sougrati, F. Jaouen, B. Halevi and S. Mukerjee, *Nano Energy*, 2016, **29**, 65−82.
25. E. F. Holby and P. Zelenay, *Nano Energy*, 2016, **29**, 54−64.
26. D. Villers, X. Jacques-Bédard and J.-P. Dodelet, *J. Electrochem. Soc.*, 2004, **151**, A1507−A1515.

27. P. Xu, W. Chen, Q. Wang, T. Zhu, M. Wu, J. Qiao, Z. Chen and J. Zhang, *RSC Adv.*, 2015, **5**, 6195−6206.
28. K. Oyaizu, E. Listiani Dewi and E. Tsuchida, *Inorg. Chim. Acta*, 2001, **321**, 205−208.
29. K. I. Ansari, J. D. Grant, G. A. Woldemariam, S. Kasiri and S. S. Mandal, *Org. Biomol. Chem.*, 2009, **7**, 926−932.
30. H. C. Sampath Kumar, B. Ramachandra Bhat, B. J. Rudresha, R. Ravindra and R. Philip, *Chem. Phys. Lett.*, 2010, **494**, 95−99.
31. W. Yang, T.-P. Fellinger and M. Antonietti, *J. Am. Chem. Soc.*, 2011, **133**, 206−209.
32. T. Jawhari, A. Roid and J. Casado, *Carbon*, 1995, **33**, 1561−1565.
33. Y. Wang, D. C. Alsmeyer and R. L. McCreery, *Chem. Mater.*, 1990, **2**, 557−563.
34. L. S. Panchakarla, K. S. Subrahmanyam, S. K. Saha, A. Govindaraj, H. R. Krishnamurthy, U. V. Waghmare and C. N. R. Rao, *Adv. Mater.*, 2009, **21**, 4726−4730.
35. Z. Jin, J. Yao, C. Kittrell and J. M. Tour, *ACS Nano*, 2011, **5**, 4112−4117.
36. D. Ye, S.Q. Wu, Y. Yu, L. Liu, X.P. Lu and Y. Wu, *Appl. Phys. Lett.*, 2014, **104**, 103105
37. J. Maruyama and I. Abe, *Chem. Mater.*, 2005, **17**, 4660−4667.
38. J. Maruyama and I. Abe, *Chem. Mater.*, 2006, **18**, 1303−1311.
39. S. Nagakura, *J. Phys. Soc. Jpn.*, 1959, **14**, 186−195.
40. K. H. Jack and S. Wild, *Nature*, 1966, **212**, 248−250.
41. J. D. Hanawalt, H. W. Rinn and L. K. Frevel, *Ind. Eng. Chem., Anal. Ed.*, 1938, **10**, 457−512.
42. L. D. Mansker, Y. Jin, D. B. Bukur and A. K. Datye, *Appl. Catal., A*, 1999, **186**, 277−296.
43. K. J. Carroll, D. M. Hudgins, S. Spurgeon, K. M. Kemner, B. Mishra, M. I. Boyanov, L. W. Brown, M. L. Taheri and E. E. Carpenter, *Chem. Mater.*, 2010, **22**, 6291−629.
44. D. Singh, J. Tian, K. Mamtani, J. King, J. T. Miller and U. S. Ozkan, *J. Catal.*, 2014, **317**, 30−43.
45. U. Tylus, Q. Jia, K. Strickland, N. Ramaswamy, A. Serov, P. Atanassov and S. Mukerjee, *J. Phys. Chem. C*, 2014, **118**, 8999−9008.
46. Q. Jia, N. Ramaswamy, H. Hafiz, U. Tylus, K. Strickland, G. Wu, B. Barbiellini, A. Bansil, E. F. Holby, P. Zelenay and S. Mukerjee, *ACS Nano*, 2015, **9**, 12496−12505.
47. U. I. Kramm, I. Herrmann-Geppert, J. Behrends, K. Lips, S. Fiechter and P. Bogdanoff, *J. Am. Chem. Soc.*, 2016, **138**, 635−640.
48. J. R. Pels, F. Kapteijn, J. A. Moulijn, Q. Zhu and K. M. Thomas, *Carbon*, 1995, **33**, 1641−1653.
49. A. Onoda, Y. Tanaka, T. Ono, S. Takeuchi, A. Sakai and T. Hayashi, *J. Porphyrins Phthalocyanines*, 2015, **19**, 510−516.
50. B. Ravel and M. Newville, *J. Synchrotron Rad.*, 2005, **12**, 537−547.

Chapter 3

Bimetallic M/N/C catalysts prepared from π-expanded metal salen precursors toward an efficient oxygen reduction reaction

3-1. Introduction

Electrochemical reduction of O_2 is a pivotal reaction for improving the performance of energy conversion devices such as fuel cells, metal-air batteries, and electrolyzers.[1-3] In particular, polymer electrolyte fuel cells (PEFCs) have been recognized as efficient energy converters enabling low emissions and low environmental impacts. Precious metal group (PMG) catalysts have been the most widely used catalysts for the cathodic oxygen reduction reaction (ORR) in PEFCs.[4-6] However, the high cost and low abundance of precious metals have been the main obstacles facing widespread commercialization of PEFCs. Thus, extensive investigations have been reported for development of alternative low-cost non-precious metal catalysts (NPMCs).[7-9]

Catalysts including a first row transition metal, such as Fe, Cu, or Co, and nitrogen atoms embedded within a carbonaceous structure are known as M/N/C catalysts and have been generally considered to represent promising alternatives to PGM catalysts, because the M/N/C catalysts have been shown to promote high levels of ORR activity while having suitable durability for use in PEFCs.[10-15] Pyrolyzed transition metals such as Fe, Cu, and Co in combination with macrocyclic ligands adsorbed on carbon supports have been proven to improve ORR activity and stability under acidic conditions, which is a requirement for PEFCs.[16, 17] A series of low-cost nitrogen-containing precursors such as phenanthroline,[11] polypyrrole,[10] and polyaniline[12] have been utilized in preparation of M/N/C catalysts. The exact chemical structures of the metal-containing active sites in the M/N/C catalysts prepared by pyrolysis remain under debate,[18, 19] although a metal and nitrogen-containing active site structure has been proposed as a catalytic site on the basis of data obtained from various spectroscopic techniques.[20-23] It is believed that metals coordinated by the N-groups play important roles in enhancement of the ORR activity of M/N/C catalysts.[11, 24]

Inspired by cytochrome *c* oxidase, which catalyzes O_2 reduction using a unique bimetallic Fe and Cu active site with ultimate efficiency, a number of examples of construction of bimetallic M/N/C catalysts containing first row transition metals as active sites have been reported.[25-32] In the enzyme, the active site containing heme iron and a copper ion is known to efficiently promote four-electron reduction of a bound O_2 molecule to water. Thus, M/N/C catalysts prepared from two precursors with two metal ions have been investigated in attemps to improve the ORR activity.[33-35]

Previously, the author reported preparation of Fe/N/C catalysts having high ORR activity by systematically tuning an aromatic framework of Fe(salen) complex precursors.[36] He demonstrated that the designed Fe(salen) derivatives with various aromatic moieties such as 1NAPD and 2NAPD ligands have higher thermal stability, which affects the annulation process of the complexes during pyrolysis, thereby leading to higher ORR activity. In this work, he describe preparation and characterization of new bimetallic FeM/N/C catalysts via pyrolysis of the π-expanded metal salen complexes (M(2NAPD) and measurement of their ORR activity. It is found that combining the M(2NAPD) precursors, in particular Fe and Cu, leads to a positive shift of onset potentials of the ORR activity of the pyrolyzed bimetallic M/N/C catalysts.

3-2. Results and Discussion

Preparation of FeM/N/C catalysts.

A series of M(2NAPD) complex precursors with expanded aromatic ligand frameworks were synthesized according to the literature (Figure 3-1a).[37-40] The thermal decomposition temperature (T_D) value of *N*,*N*´-bis(2-hydroxy-1-naphthylidene)-1,2-phenylenediaminoiron(III) chloride (Fe(2NAPD)) containing the expanded aromatic ring framework is 417 °C. This is shifted more than 84 °C above the T_D value of Fe(salen). Therefore, he prepared additional corresponding metal complexes Cu(2NAPD), Co(2NAPD), Ni(2NAPD) and Mn(2NAPD) as catalyst precursors. The thermogravimetric analysis of the precursors indicates that the aromatic rings in the ligand frameworks also enhance the thermal stability of Cu(2NAPD), Co(2NAPD), Ni(2NAPD), and Mn(2NAPD) complexes during pyrolysis (Table 3-1, Figure 3-2).

The M/N/C electrocatalysts were prepared by pyrolysis of the mixture of M(2NAPD) complexes and carbon black Vulcan XC-72R (VC, Cabot, USA)(Figure 3-1b). One or two types of the M(2NAPD) complex dissolved in $CHCl_3$ were vigorously mixed with VC and the solvent was removed to afford the precursor. The obtained precursor was preheated to 300 °C for 1 h and then incubated at 300 °C for 2 h

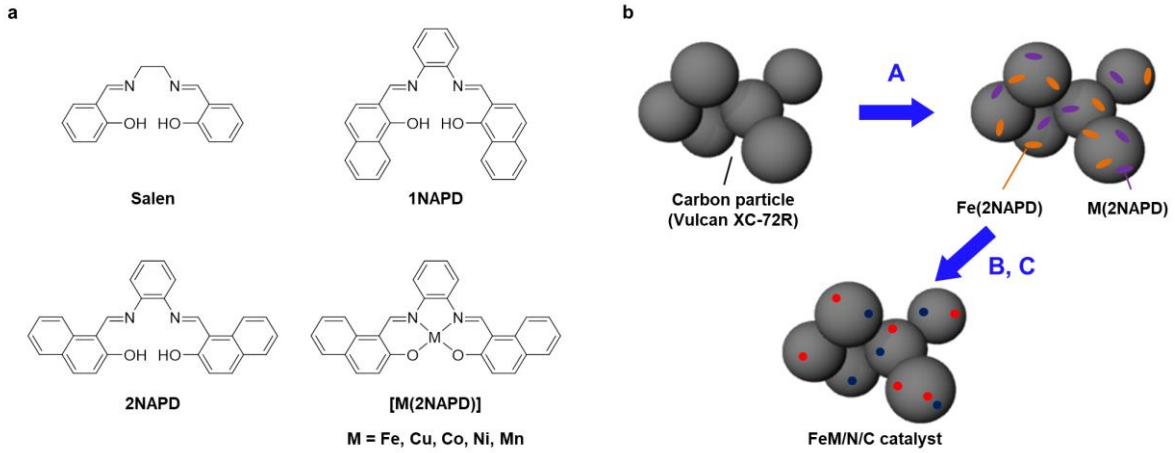

Figure 3-1. (a) Structures of Salen, 1NAPD, 2NAPD ligand and M(2NAPD) complexes. (b) The scheme for preparation of bimetallic FeM/N/C catalysts. (A) mixing of Fe(2NAPD) complex (orange) and M(2NAPD) complex (purple) with carbon materials, (B) pyrolysis at 1000 ºC under N_2 atmosphere, and (C) treatment with H_2SO_{4aq} to remove metal impurities and to prepare the FeM/N/C catalysts containing the iron (red) and other metal (dark blue) active sites.

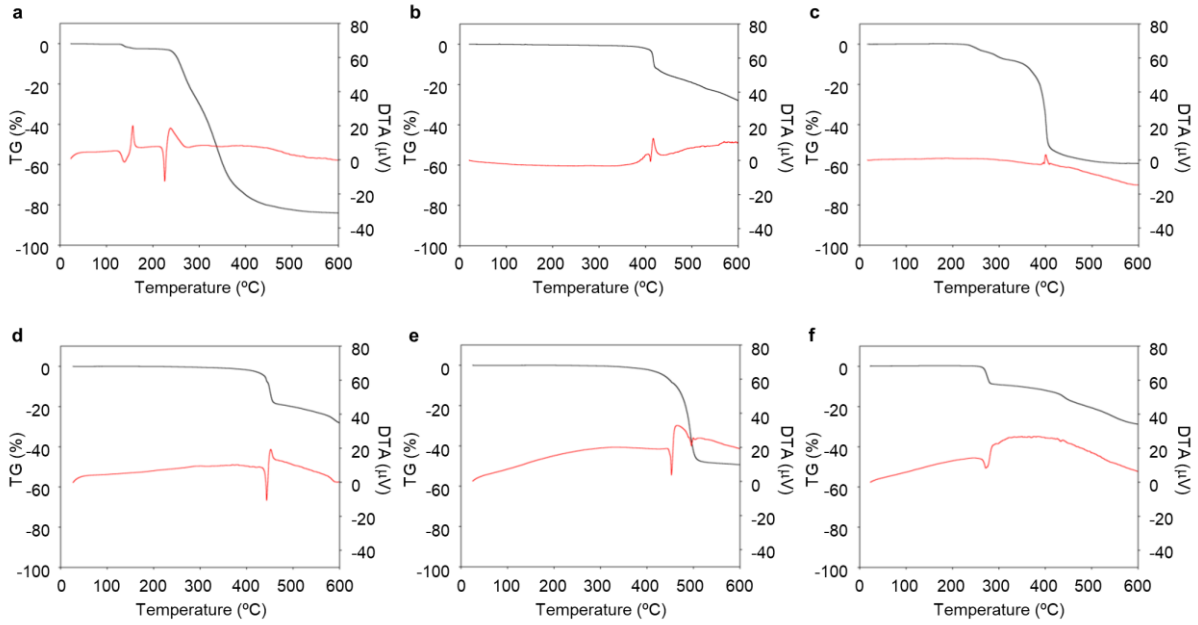

Figure 3-2. Thermogravimetric-differential thermal analysis of M(2NAPD) precursors. Thermal gravimetric analysis curves (black) and differential thermal analysis curves (red) of M(2NAPD) precursors. (a) 2NAPD, (b) Fe(2NAPD)Cl, (c) Cu(2NAPD), (d) Co(2NAPD), (e) Ni(2NAPD), and (f) Mn(2NAPD).

under constant N_2 gas flow. The carbon materials were immediately pyrolyzed at 1000 °C for 2 h under constant N_2 gas flow for carbonization. The pyrolyzed powder was ground and leached in an acidic solution (0.5 M H_2SO_4) to remove metal species such as metal oxides and unincorporated metal species. After washing twice with an excess of water and drying, Fe/2NAPD@VC, Cu/2NAPD@VC, Co/2NAPD@VC,

Ni/2NAPD@VC, Mn/2NAPD@VC, FeCu/2NAPD@VC, FeCo/2NAPD@VC, FeNi/2NAPD@VC, and FeMn/2NAPD@VC were produced. These materials were characterized by elemental analysis, inductively coupled plasma atomic emission spectrometry (ICP-AES), X-ray diffraction (XRD), and Raman spectroscopy, and X-ray photoelectron spectroscopy (XPS).

ORR Activity

The ORR activities of the M/N/C and bimetallic FeM/N/C catalysts were determined using a rotating disk electrode at different rotation rates in a medium of O_2-saturated 0.1 M $HClO_4$ at pH 1 (Figures 3-3a and 3-3b). M/N/C and FeM/N/C catalysts prepared from the M(2NAPD) precursors show significant cathodic current during O_2 reduction, indicating high levels of ORR activity. The number of electrons transferred during O_2 reduction (n) was determined from Koutecky-Levich plots for each carbon catalyst (Tables 3-1 and 3-2, Figures 3-3c and 3-3d).

First, in the case of the monometallic M/N/C catalyst, as the author reported previously, the onset potentials of the Fe/N/C catalysts shift positively for the catalyst prepared from the Fe(salen) complex with the π-expanded ligand framework. In particular, Fe/2NAPD@VC has a significantly shifted onset potential, suggesting that introduction of aromatic rings into the ligand framework of the precursor positively shifts the onset potential in Fe/2NAPD@VC relative to Fe/Salen@VC.[36] Among the M/N/C catalysts prepared in this work, Fe/2NAPD@VC has the most shifted positive onset potentials (0.82 V) relative to the onset potentials of other catalysts including Cu/2NAPD@VC, Co/2NAPD@VC, Ni/2NAPD@VC, and Mn/2NAPD@VC (Table 3-1). The average number of electrons transferred during O_2 reduction is 3.6 for Fe/2NAPD@VC, generally indicating occurrence of four electron reduction. Both Cu/2NAPD@VC and Co/2NAPD@VC also show moderate activity for four electron reduction. In contrast, Ni/2NAPD@VC and Mn/2NAPD@VC promote two electron reduction as well as metal-free 2NAPD@VC.

On the basis of the electrochemical result showing high electrocatalytic ORR activity for Fe/2NAPD@VC, the author prepared bimetallic FeM/N/C catalysts using Fe(2NAPD) and other M(2NAPD) complexes as precursors and their electrocatalytic properties were analyzed. The onset potentials of FeCu/2NAPD@VC, FeCo/2NAPD@VC, FeNi/2NAPD@VC, and FeMn/2NAPD@VC are 0.87 V, 0.83 V, 0.76 V, and 0.69 V, respectively (Table 3-2). Interestingly, the onset potential (0.87 V) of FeCu/2NAPD@VC exhibits remarkable positive shifts relative to the onset potential of Fe/2NAPD@VC (0.82 V). In addition, FeCo/2NAPD@VC also has a slightly

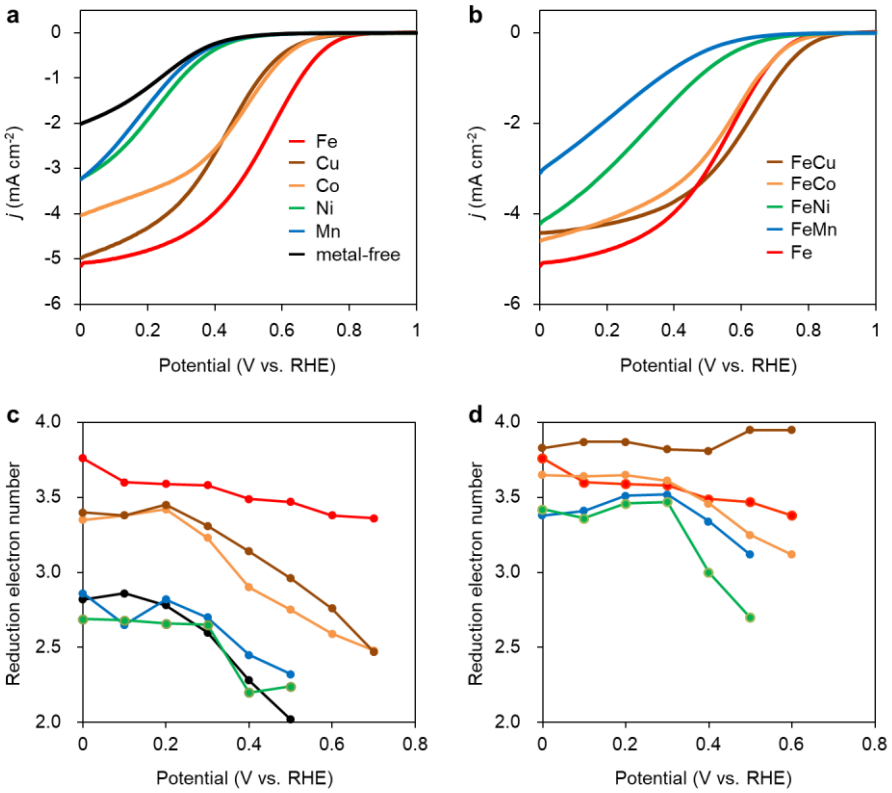

Figure 3-3. (a) ORR polarization curves of M/N/C catalysts; Fe/2NAPD@VC (red), Cu/2NAPD@VC (brown), Co/2NAPD@VC (orange), Ni/2NAPD@VC (green), Mn/2NAPD@VC (blue), and metal-free 2NAPD@VC (black). (b) ORR polarization curves of FeM/N/C catalysts; FeCu/2NAPD@VC (brown), FeCo/2NAPD@VC (orange), FeNi/2NAPD@VC (green), FeMn/2NAPD@VC (blue), and Fe/2NAPD@VC (red) in O_2-saturated 0.1 M $HClO_4$ solution at 5 $mV \cdot s^{-1}$ with 2000 rpm. (c) the number of electrons transferred during O_2 reduction of M/N/C catalysts; Fe/2NAPD@VC (red), Cu/2NAPD@VC (brown), Co/2NAPD@VC (orange), Ni/2NAPD@VC (green), Mn/2NAPD@VC (blue), and metal-free 2NAPD@VC (black). (d) the number of electrons transferred during O_2 reduction of FeM/N/C catalysts; FeCu/2NAPD@VC (brown), FeCo/2NAPD@VC (orange), FeNi/2NAPD@VC (green), FeMn/2NAPD@VC (blue), and Fe/2NAPD@VC (red).

shifted onset potential (0.83 V). Furthermore, the *n* value of FeCu/2NAPD@VC (3.9) is higher than that of Fe/2NAPD@VC (3.6). The results clearly indicate that the bimetallic catalyst FeCu/2NAPD@VC promotes four electron reduction of O_2 and has higher activity relative to that of monometallic Fe/2NAPD@VC and Cu/2NAPD@VC. The author also found that the 1:1 ratio of the Fe and Cu 2NAPD complexes has the best activity (Figure 3-4a). Furthermore, the bimetallic Fe/Cu carbon catalyst prepared from the mixture of simple Fe and Cu salen complexes has a negatively shifted onset potential of 0.77 V (Figure 3-4b). The diffusion-limited current density of FeCu/2NAPD@VC is slightly decreased relative to that of Fe/2NAPD@VC. In general, it is known that the diffusion-limited current density depends not only on the activity but also on the electrochemical active surface area (EASA), which is related to C_{dl}, the electrochemical

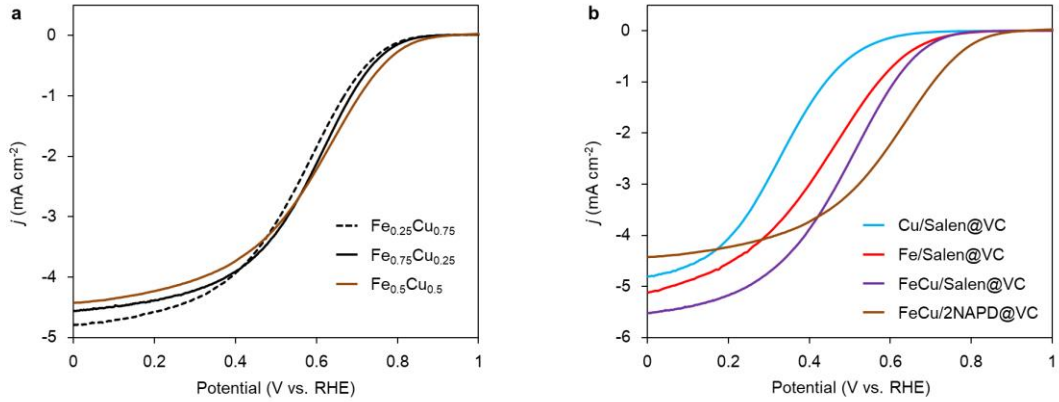

Figure 3-4. ORR polarization curves of FeCu/2NAPD@VC catalyst and the reference samples. (a) Influence of the ratio of Fe precursor to Cu precursor. $Fe_{0.25}Cu_{0.75}$/2NAPD@VC (dashed black line), $Fe_{0.75}Cu_{0.25}$/2NAPD@VC (black line), and FeCu/2NAPD@VC (brown). $Fe_{0.25}Cu_{0.75}$/2NAPD@VC and $Fe_{0.75}Cu_{0.25}$/2NAPD@VC catalysts were prepared from 21 μmol of Fe precursor and 63 μmol of Cu precursor, 63 μmol of Fe precursor and 21 μmol of Cu precursor. The onset potentials are 0.83 V ($Fe_{0.25}Cu_{0.75}$/2NAPD@VC), 0.84 V ($Fe_{0.75}Cu_{0.25}$/2NAPD@VC), and 0.87 V (FeCu/2NAPD@VC). (b) Influence of the π-expanded salen ligand (2NAPD). Cu/Salen@VC (blue), Fe/Salen@VC (red), FeCu/Salen@VC (purple), the catalysts prepared from M(Salen) complexes with simple salen ligand, and FeCu/2NAPD@VC (brown). The onset potentials are 0.66 V (Cu/Salen@VC), 0.73 V (Fe/Salen@VC), 0.77 V (FeCu/Salen@VC), and 0.87 V (FeCu/2NAPD@VC).

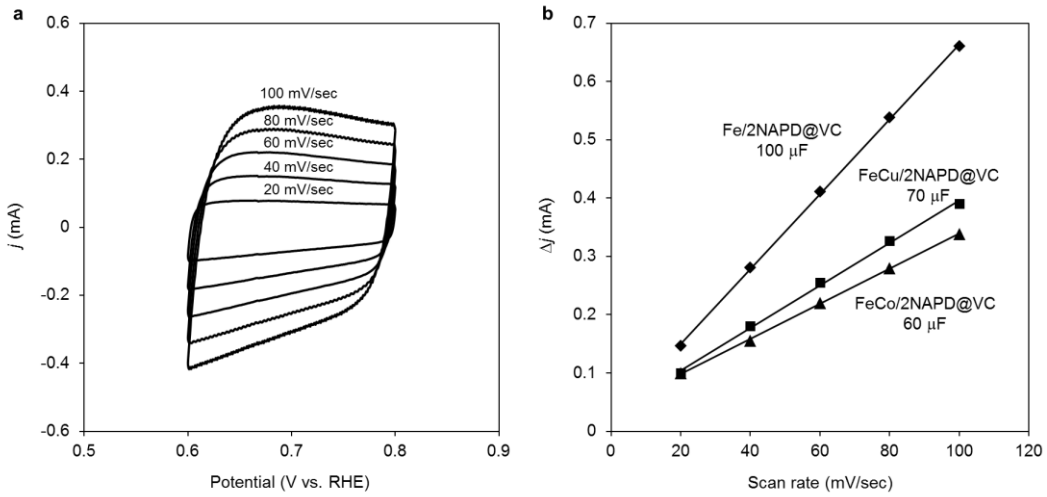

Figure 3-5. Cyclic voltammograms of Fe/2NAPD@VC in the potential range of 0.6 V to 0.8 V (vs. RHE) at the scan rates of 20, 40, 60, 80, and 100 mV/sec in N_2-saturated 0.1 M $HClO_4$ solution. (b) The differences in current variations ($\Delta j = j_a - j_c$) of Fe/2NAPD@VC, FeCu/2NAPD@VC, and FeCo/2NAPD@VC at 0.7 V (vs. RHE) plotted against scan rate fitted to a linear regression for the calculation of C_{dl}.

double-layer capacitance of the catalytic surface. The C_{dl} value of Fe/2NAPD@VC is determined to be 100 μF, which is higher than that of FeCu/2NAPD@VC (70 μF) (Figure 3-5). Therefore, the larger C_{dl} value of Fe/2NAPD@VC explains the larger diffusion-limited current density.These findings indicate that the ORR catalysts prepared from the mixed M(2NAPD) precursors have a synergistic effect provided by bimetallic active sites, which efficiently proceed four-electron reduction.

Characterization of the M/N/C and FeM/N/C catalysts

The carbon materials in the monometallic M/N/C and bimetallic FeM/N/C catalysts were first analyzed by Raman spectroscopy (Figures 3-6a and 3-7a). It is known that a disordered carbon structure has significantly different spectra with a D (disorder) band in the vicinity of 1355 cm^{-1}. Graphitized carbons give rise to a G (graphite) band in the vicinity of 1580 cm^{-1}, which is assignable to in-plane displacement of carbon strongly coupled in the hexagonal sheets.[41, 42] The Raman spectra of the M/N/C and bimetallic FeM/N/C catalysts presenting typical D- and G-bands indicate that the disordered carbonaceous structure is included in these catalysts. The integrated intensity ratio I_D/I_G for the D-band and G-band is widely used to quantify defects in graphitic materials. The I_D/I_G ratio for all monometallic M/N/C and bimetallic FeM/N/C catalysts is approximately 1.1, suggesting that all catalysts include similar graphitic and disordered structural content in the carbonaceous materials. The nitrogen-doped graphene has been known to have D' peak near 1600 cm^{-1}.[43-45] The G band peaks for the M/N/C catalysts are located at 1600 cm^{-1}, which represents a shift from the peak at 1583 cm^{-1} for VC without nitrogen atom and for VC pyrolyzed with the 2NAPD ligand. This result indicates that nitrogen atoms are doped in the carbon framework in accordance with the metal species.

X-ray diffraction (XRD) experiments were performed to confirm each carbonaceous structure of the M/N/C and FeM/N/C catalysts prepared from the M(2NAPD) complexes and the chemical composition of the metal species (Figures 3-6b and 3-7b). In general, powder samples of carbons in an amorphous structure provide diffraction peaks for (002) (2θ = *ca.* 26.0°), and (101) (2θ = *ca.* 44.0°).[46, 47] The carbon catalysts were found to exhibit a strong and broad peak at ca. 26.0° and a weak and broad peak at 44.0°. In addition, the peaks for Co/2NAPD@VC (2θ = 43.9° and 51.2°), FeCu/2NAPD@VC (2θ = 43.3° and 50.5°), FeCo/2NAPD@VC (2θ = 45.1°), and FeNi/2NAPD@VC (2θ = 43.6° and 50.8°) indicate that Co metal,[48] FeCu,[49] FeCo,[50] and FeNi alloys[51] are generated in each catalyst.

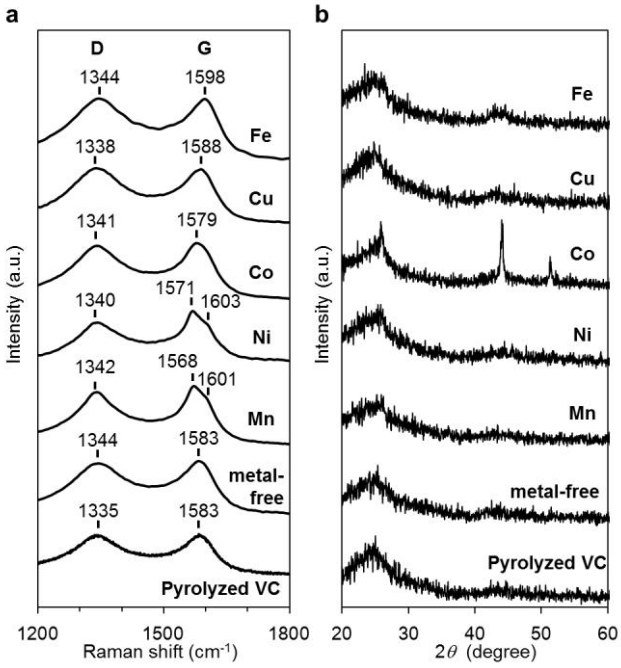

Figure 3-6. Characterization of the M/N/C catalysts prepared from M(2NAPD) precursors. (a) Raman spectra and (b) XRD patterns of Fe/2NAPD@VC, Co/2NAPD@VC, Ni/2NAPD@VC, Mn/2NAPD@VC, 2NAPD@VC, and pyrolyzed VC.

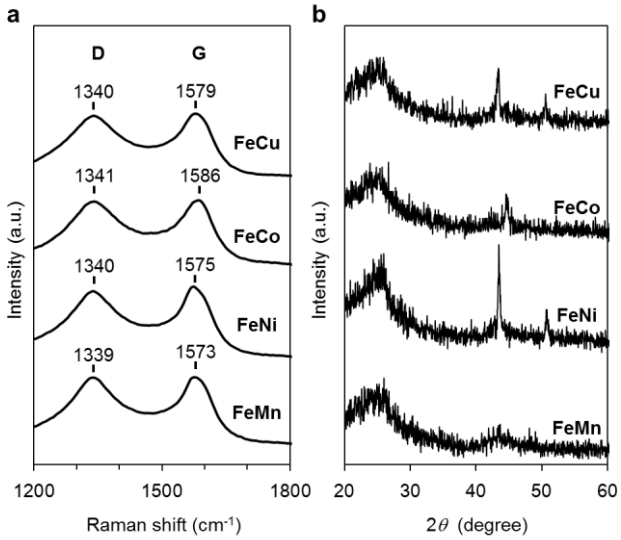

Figure 3-7. Characterization of the FeM/N/C catalysts prepared from M(2NAPD) precursors. (a) Raman spectra and (b) XRD patterns of FeCu/2NAPD@VC, FeCo/2NAPD@VC, FeNi/2NAPD@VC, and FeMn/2NAPD@VC.

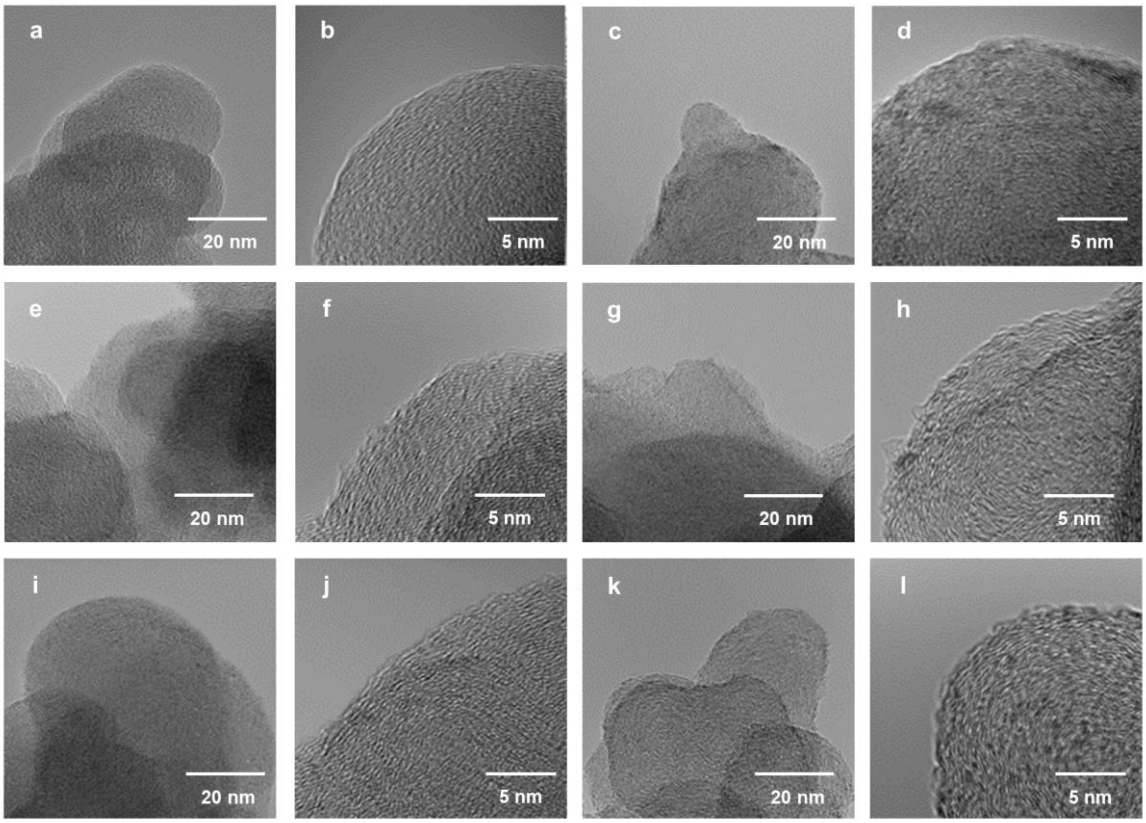

Figure 3-8. HRTEM images of (a,b) 2NAPD@VC, (c,d) Fe/2NAPD@VC, (e,f) Cu/2NAPD@VC, (g,h) Co/2NAPD@VC, (i,j) Ni/2NAPD@VC, and (k,l) Mn/2NAPD@VC. (magnification = 300k and 1000k) The metal content of each of the samples determined by EDS analysis with an electron probe of 25 nm in the area with 300k magnification is (c) Fe: 0.79 wt%, (e) Cu: 0.80 wt%, (g) Co: 0.19 wt%, (i) Ni: 0.72 wt%, and (k) Mn: 0.54 wt%.

The content of metal and N atoms in the M/N/C and FeM/N/C catalysts was determined by elemental analysis with ICP-AES measurements. The elemental compositions of the Fe/N/C and FeM/N/C catalysts are summarized in Tables 3-1 and 3-2 together with other properties. The content of the metal ranges between 1.2−0.1%. Therefore, the metals of the precursors are retained in the carbonaceous structure after treatment of an aqueous H_2SO_4solution at 80 °C to remove the metal nanoparticles and metal oxides. In addition, the nitrogen content of the M/N/C catalysts is higher than that of the 2NAPD@VC catalyst prepared from 2NAPD without metal (0.3%). This suggests that the larger amount of the nitrogen species is incorporated into the carbonaceous structure by the pyrolysis of the metal salen precursors.

High resolution transmission electron microscope (HRTEM) images of the M/N/C and FeM/N/C catalysts were obtained to determine the nanostructures of the catalyst (Figures 3-8 and 3-9). The M/N/C catalysts are found to have a spherical form with diameters ranging from 40 to 70 nm, which are retained in the structure of VC. The author confirmed the existence of each metal in the carbon structure by performing chemical composition analyses using EDS (Energy dispersive X-ray spectrometry). The data are in good

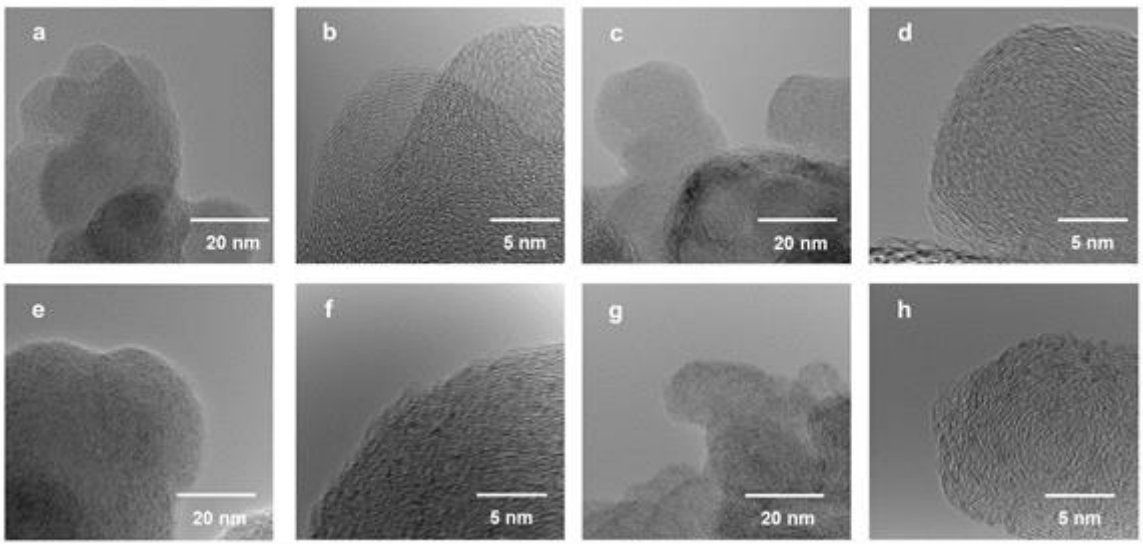

Figure 3-9. HRTEM images of (a,b) FeCu/2NAPD@VC, (c,d) FeCo/2NAPD@VC, (e,f) FeNi/2NAPD@VC, and (g,h) FeMn/2NAPD@VC. (magnification = 300k and 1000k) The metal content of each of the samples determined by EDS analysis with an electron probe of 25 nm in the area with 300k magnification is (a) Fe: 0.31 wt%, Cu: 0.18 wt%, (c) Fe: 0.33 wt%, Co: 0.16 wt%, (e) Fe: 0.33 wt%, Ni: 0.16 wt%, and (g) Fe: 0.40 wt%, Mn: 0.27 wt%.

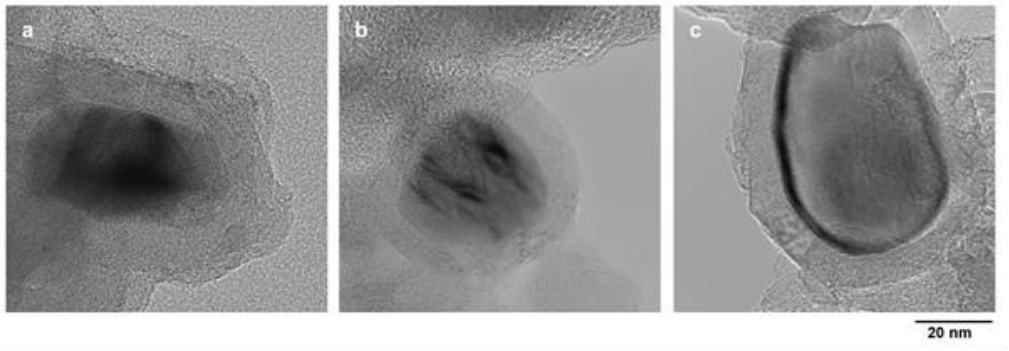

Figure 3-10. HRTEM images of (a,b) FeCu/2NAPD@VC, (c,d) FeCo/2NAPD@VC, (e,f) FeNi/2NAPD@VC, and (g,h) FeMn/2NAPD@VC. (magnification = 300k and 1000k) The metal content of each of the samples determined by EDS analysis with an electron probe of 25 nm in the area with 300k magnification is (a) Fe: 0.31 wt%, Cu: 0.18 wt%, (c) Fe: 0.33 wt%, Co: 0.16 wt%, (e) Fe: 0.33 wt%, Ni: 0.16 wt%, and (g) Fe: 0.40 wt%, Mn: 0.27 wt%.

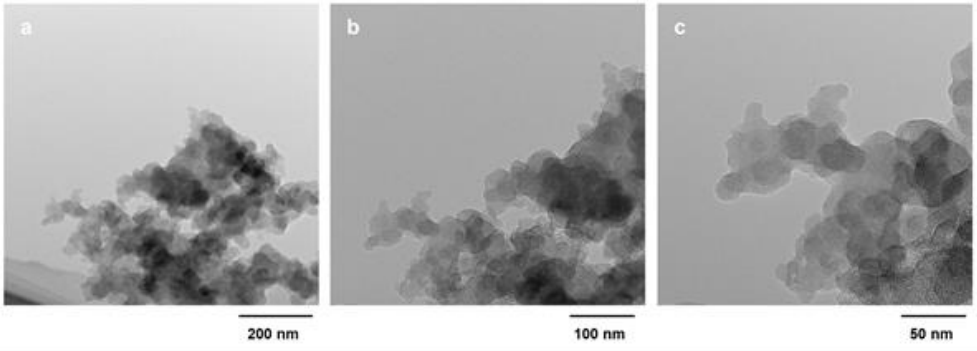

Figure 3-11. HRTEM images of FeCu/2NAPD@VC with low magnification. (a) 30k, (b) 50k, and (c) 100k.

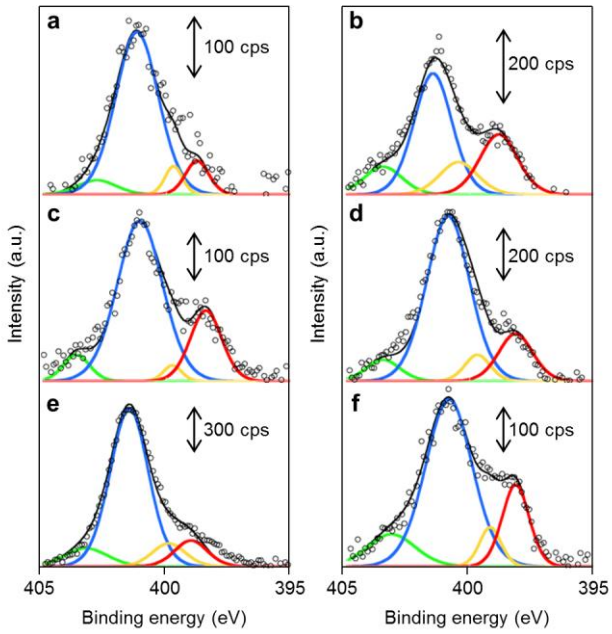

Figure 3-12. The distribution of pyridinic N, pyrrolic N, graphitic N and *N*-oxide in M/N/C catalysts. XPS spectra of (a) 2NAPD@VC, (b) Fe/2NAPD@VC, (c) Cu/2NAPD@VC, (d) Co/NAPD@VC, (e) Ni/2NAPD@VC, and (f) Mn/2NAPD@VC in the N1s region with fitted peaks of pyridinic-N (red), pyrrolic-N (yellow), graphitic-N (blue), and *N*-oxide (green).

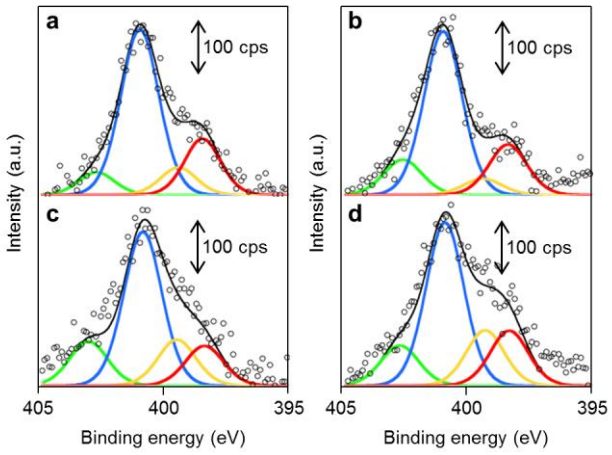

Figure 3-13. The distribution of pyridinic N, pyrrolic N, graphitic N and *N*-oxide in FeM/N/C catalysts. XPS spectra of (a) FeCu/2NAPD@VC, (b) FeCo/2NAPD@VC, (c) FeNi/2NAPD@VC, and (d) FeMn/2NAPD@VC in the N1s region with fitted peaks of pyridinic-N (red), pyrrolic-N (yellow), graphitic-N (blue), and *N*-oxide (green).

accordance with the data obtained from the ICP-AES measurements. Therefore, the main components of metals are highly dispersed in the carbon structure in each catalyst. In the case of Co/2NAPD@VC, FeCo/2NAPD@VC, and FeNi/2NAPD@VC, the author also observed nanoparticles of Co metal, FeCo, and FeNi alloys, respectively in HRTEM images (Figure 3-10). In contrast, such nanoparticle of FeCu

Table 3-1. Characterization and electrochemical activity of M/N/C catalysts.

M/N/C catalyst	T_D[a] (ºC)	BET (m^2/g)	Elemental analysis		XPS (N1s)				E_{onset}[c] (V)	n[d]
			M[b] (wt%)	N (wt%)	Pyridinic (%)	Pyrrolic (%)	Graphitic (%)	*N*-oxide (%)		
Fe/2NAPD@VC	417	143	0.9	0.8	24.9	13.4	50.2	11.5	0.82	3.6
Cu/2NAPD@VC	396	422	1.1	0.4	21.2	2.8	69.5	6.6	0.76	3.3
Co/2NAPD@VC	435	294	1.2	0.7	16.0	6.5	70.5	7.0	0.74	3.2
Ni/2NAPD@VC	445	362	0.8	0.9	10.1	9.0	71.8	9.2	0.55	2.7
Mn/2NAPD@VC	264	328	0.2	0.6	17.8	6.8	63.1	12.3	0.54	2.7
2NAPD@VC	230	801	-	0.3	8.9	5.6	79.3	6.2	0.53	2.6

[a] Decomposition temperature of M(2NAPD) precursors determined by TG-DTA. [b] Determined by ICP-AES. [c] The potential at I = 0.05 mA·cm^{-2} in RDE. [d] The number of electrons transferred during O_2 reduction calculated by Koutecky−Levich plots at 0.3 V.

Table 3-2. Characterization and electrochemical activity of FeM/N/C catalysts.

FeM/N/C catalyst	BET (m^2/g)	Elemental analysis		XPS (N1s)				E_{onset}[c] (V)	n[d]
		M[a] (wt%)	N (wt%)	Pyridinic (%)	Pyrrolic (%)	Graphitic (%)	*N*-oxide (%)		
FeCu/2NAPD@VC	447	1.2	0.7	0.8	20.0	9.7	62.3	8.0	0.87
FeCo/2NAPD@VC	631	0.4	0.2	0.5	18.9	6.1	61.7	13.3	0.83
FeNi/2NAPD@VC	896	1.1	0.5	0.7	14.0	16.2	54.3	15.6	0.76
FeMn/2NAPD@VC	1095	0.6	0.1	0.5	17.5	17.6	52.0	12.8	0.69

[a] Determined by ICP-AES. [b] The potential at I = 0.05 mA·cm^{-2} in RDE. [c] The number of electrons transferred during O_2 reduction calculated by Koutecky−Levich plots at 0.3 V.

alloys were not observed at all in the FeCu/N/C catalyst (Figure 3-11), which shows a similar trend observed in Fe/2NAPD@VC and Cu/2NAPD@VC. Considering the existence of the FeCu alloy structure in XRD analysis, the results indicate that highly dispersed FeCu alloys are generated in FeCu/2NAPD@VC, which has the highest activity in four electron reduction of O_2.

XPS measurements

The chemical structures of the nitrogen atoms in the M/N/C and FeM/N/C catalysts were determined by X-ray photoelectron spectroscopy (XPS) measurements (Figures 3-12 and 3-13). Four types of nitrogen species are confirmed by the N1s peaks in the range between 398.0 and 404.0 eV.[52, 53] The N1s spectra were deconvoluted into four different nitrogen species including

pyridinic N (398.0-398.9 eV), pyrrolic N (399.5−400.4 eV), graphitic N (400.5−402.0), and *N*-oxide groups (N^+–O^-) at binding energies higher than 402.0 eV. The content is summarized in Tables 1 and 2. Interestingly, the content of pyridinic N of Fe/2NAPD@VC (24.9%) and Cu/2NAPD@VC (21.2%) is higher than that of the catalyst prepared from 2NAPD (8.9%). This indicates that the pyridinic moiety in the carbonaceous structure is important to bind the metal active sites in the catalysts. This is consistent with the reported evidence that metals coordinated by the N-groups play important roles in enhancement of the ORR activity of M/N/C catalysts.[11, 24] The author found that the nitrogen content (0.8 wt%) and the pyridinic nitrogen content (20%) for FeCu/2NAPD@VC are higher than those of other catalysts. Since the catalysts are treated in acid during the preparation, only the carbon-encapsulated metal or metal alloy nanoparticles remain in the carbonaceous structure. Therefore, he expect that the N-coordinated Fe and Cu sites, which are highly dispersed in the carbonaceous structure, are the active sites promoting efficient four-electron reduction of O_2 in the FeCu/2NAPD@VC catalyst.

3-3. Conclusions

This work demonstrates a new method for improving the ORR activity of bimetallic M/N/C catalysts using mixed metal precursors containing π-expanded ligand frameworks. The bimetallic FeM/N/C catalysts were prepared by pyrolysis of the mixture of carbon support and the M(2NAPD) precursors. The catalyst prepared using the Fe(2NAPD) complex with π-expanded ligand framework exhibits a remarkable positive shift in the onset potential for ORR relative to catalysts prepared from the M(2NAPD) complex (M = Cu, Co, Ni, Mn). By mixing these heterometallic precursors, the author found that ORR activity can be significantly improved. In particular, FeCu/2NAPD@VC has a positively-shifted onset potential for ORR with excellent four-electron O_2 reduction activity. Both Fe and Cu metals together with pyridinic nitrogen species are highly dispersed within the carbonaceous structure in FeCu/2NAPD@VC, suggesting that the N-coordinated Fe and Cu sites promote efficient four-electron reduction of O_2. These findings prove that this approach of using aromatic ligand frameworks for metal precursor complexes contributes to enhancement of ORR activity of non-precious bimetallic M/N/C catalysts which are appropriate for incorporation into fuel cells and metal-air battery applications.

3-4. Experimental Section

Materials

All reagents were used without purification. All solvents were dried with molecular sieves 3A before use.

Synthesis of M(2NAPD) complexes

Metal ion was inserted to the 2NAPD ligand by mixing 1 equivalent of metal salt ($FeCl_3$, $Cu(OAc)_2$, $Co(OAc)_2$, $Ni(OAc)_2$ or $Mn(OAc)_2$) in 300 mL of ethanol/acetone (1/1, v/v). The reaction mixture was refluxed for 2 h, and cooled to room temperature. The precipitates were collected by filtration, washed with a small portion of ethanol, and dried to yield the products.

[Fe(2NAPD)Cl]. Yield: 69%; UV-vis (DMSO, nm): 334, 397, 453; ESI-TOF MS (positive mode) *m/z* calcd for $C_{28}H_{18}FeN_2O_2$ $[M]^+$ 470.07, found 470.07.

[Cu(2NAPD)]. Yield: 87%; UV-vis (DMSO, nm): 336, 429, 466; ESI-TOF MS (positive mode) *m/z* calcd for $C_{28}H_{18}CuN_2O_2$ $[M+Na]^+$ 500.06, found 500.05.

[Co(2NAPD)]. Yield: 92%; UV-vis (DMSO, nm): 346, 420; ESI-TOF MS (positive mode) *m/z* calcd for $C_{28}H_{18}CoN_2O_2$ $[M]^+$ 473.07, found 473.06.

[Ni(2NAPD)]. Yield: 96%; UV-vis (DMSO, nm): 331, 387, 484; ^{1}H NMR (400 MHz, DMSO-d_6) δ 9.42 (2H, s, N=C*H*), 8.56 (2H, d, *J* = 8.6 Hz, 8-*H*), 8.49–8.46 (2H, m, *J* = 6.5 Hz, 4´-*H*), 7.86 (2H, d, 4-*H*), 7.81 (2H, d, *J* = 7.7 Hz, 5-*H*), 7.58 (2H, t, *J* = 7.2 Hz, 8.6 Hz, 7-*H*), 7.38–7.34 (4H, m, *J* = 6.5 Hz, 7.2 Hz, 7.7 Hz, 3´-*H*, 6-*H*), 7.15 (2H, d, *J* = 9.3 Hz, 3-*H*).

[Mn(2NAPD)]. Yield: 83%; UV-vis (DMSO, nm): 375, 453, 482; ESI-TOF MS (positive mode) *m/z* calcd for $C_{28}H_{18}FeN_2O_2$ $[M]^+$ 469.07, found 469.07.

Catalyst preparation

Carbon black Vulcan XC-72R (VC, Cabot, USA) was used as a carbon support. Electrocatalysts were prepared from M(2NAPD) complexes and VC by pyrolysis in N_2 flow. The electrocatalysts, which are abbreviated as M/2NAPD@VC and FeM/2NAPD@VC, were prepared as follows: Fe(2NAPD) (42 mg, 84 μmol) was dissolved in a minimum volume of $CHCl_3$ and mixed with a powder of VC (30 mg). The suspension was vigorously vortexed and sonicated for 30 min. After removal of the solvent, the residue was used as a precursor for an electrocatalyst.

Fe(2NAPD) (42 μmol) and M(2NAPD) (42 μmol) (M = Cu, Co, Ni, Mn) were used for FeM/2NAPD@VC. The precursor was placed on an alumina boat (length: 80 mm, width: 16 mm, height: 10 mm), and then inserted into a quartz tube (diameter 50 mm, length 800 mm). The quartz tube was installed in a hinge split tube furnace (Koyo Thermo Systems Co. Ltd., KTF045N1). The precursor was preheated from ambient temperature to 300 °C for 1 h under N_2 flow (0.2 $L \cdot min^{-1}$), and incubated for 2 h. The precursor was then heated to 1000 °C for 1 h immediately, and incubated for 2 h. The temperature of the sample inside the furnace was recorded with a thermocouple equipped with a data logger (CHINO Corporation, MC3000). After cooling, the pyrolyzed catalyst was ground and further treated in a 0.5 M H_2SO_4 solution at 80 °C for 3 h to leach out impurities such as metal oxides and then washed with excess volumes of deionized water twice. The dried carbon catalyst was used for the experiments. Other carbon catalysts (Cu/2NAPD@VC, Co/2NAPD@VC, Ni/2NAPD@VC, Mn/2NAPD@VC, 2NAPD@VC, FeCu/2NAPD@VC, FeCo/2NAPD@VC, FeNi/2NAPD@VC, and FeMn/2NAPD@VC) were obtained using the same protocol with the iron complex.

Physicochemical characterization

The decomposition temperatures of M(2NAPD) complexes were determined by themogravimetry-differential thermal analysis (TG-DTA) using a Mac Science TG-DTA TMA DSC with a heating rate of 10 °C min^{-1} under an N_2 stream in a platinum pan. Metal content of each of the M/N/C catalysts and the FeM/N/C catalysts was determined by inductively coupled plasma atomic emission spectroscopy (ICP-AES) using a SHIMAZDU ICPS-7510 system. Specific surface areas were obtained using a Quantachrome NOVA 4200e Surface Analyzer and calculated by the Brunauer−Emmett−Teller (BET) method. The Raman spectra were obtained using a JASCO NRS-3100 instrument with a 532 nm laser. X-ray diffraction (XRD) patterns of the samples were obtained using an X-ray diffractometer (Rigaku, SmartLab) equipped with a Cu Kα source. High-resolution transmission electron microscopy (HRTEM) observations and chemical composition analyses were carried out using a HITACHI HF-2000 field emission TEM operated with an accelerating voltage of 200 kV. The chemical composition of each sample was analyzed by EDS (NORAN Instruments). The analyses were carried out using an electron probe approximately 25 nm in diameter. The characteristic X-ray of metals was collected with an ultra-thin window X-ray detector at a high take-off angle of 68 degrees. The morphology of the catalysts were observed using a JEOL JSM-6335 field emission scanning electron microscope (FE-SEM) operated

at an accelerating voltage of 20 kV. XPS measurements were performed on a KRATOS AXIS-165x (SHIMADZU) system, equipped with a Mg Kα X-ray source. Individual chemical components of the N1s binding energy region were fitted to the spectra after a Tougaard-type background subtraction.

Electrochemical measurement.

A rotating disk electrode with a glassy carbon disk electrode (ϕ = 5 mm) was used for evaluation of the carbon catalysts. Electrode rotation rates were controlled using a Pine Instruments AFMSRCE rotator with a Pine MSRX motor controller. The electrode was polished to mirror flat with alumina powder (50 nm) before use. The catalyst ink included a mixture of 12.0 mg of catalyst ((Fe/2NAPD@VC, Cu/2NAPD@VC, Co/2NAPD@VC, Ni/2NAPD@VC, Mn/2NAPD@VC, 2NAPD@VC, FeCu/2NAPD@VC, FeCo/2NAPD@VC, FeNi/2NAPD@VC, or FeMn/2NAPD@VC)), and 50 μL of 5 wt% Nafion® solution (Sigma-Aldrich), and 950 μL of isopropanol. The ink was vortexed and sonicated in an ultrasonic bath at 100 W at 35 kHz for 30 min. Then 10 μL of the catalyst ink was loaded onto the surface of the electrode and dried.

Electrochemical tests were carried out on a potentiostat (ALS, electrochemical analyzer model 610B) using a typical three-electrode system, with platinum wire as a counter electrode and Ag/AgCl as a reference electrode. The potential difference between Ag/AgCl and RHE was calculated and the value is 0.258 V in a 0.1 M $HClO_4$ solution. The scan rate for all measurements was 5 $mV \cdot s^{-1}$ from −0.258 to 0.742 V versus the Ag/AgCl reference electrode. Before each potential scan, the electrolyte of the 0.1 M $HClO_4$ solution was saturated with O_2 for at least 30 min, and O_2 purging was continued during the electrochemical experiments. The measured current was subtracted from the background current at the N_2-saturated electrolyte. The number of electrons transferred during O_2 reduction was calculated using the Koutecky–Levich equation (Equations. 3-1 and 3-2)[54]

$$I^{-1} = I_K^{-1} + I_L^{-1} \qquad (3\text{-}1)$$

$$I_L = 0.620nFAD_0^{2/3}\omega^{1/2}\nu^{-1/6}C_0 \qquad (3\text{-}2)$$

where I, I_K, and I_L represent the measured, kinetically-controlled, and diffusion-limited currents, respectively. n is the number of exchanged electrons, ω is the angular frequency of rotation, $\omega = 2\pi f/60$, f is the RDE rotation rate in rpm, F is the Faraday constant (96,485 $C \cdot mol^{-1}$), D_0 is the diffusion coefficient of O_2 in 0.1 M $HClO_4$ solution (1.9 x 10^{-5} $cm^2 \cdot s^{-1}$), ν is the kinematic

viscosity of electrolyte (9.87 x 10^{-3} $cm^2 \cdot s^{-1}$), and C_0 is the concentration of O_2 (11.8 x 10^{-6} $mol \cdot cm^{-3}$). EASA of catalysts is determined by following equations (3-3, 3-4, and 3-5),

$$EASA = C_{dl}/C_s \quad (3\text{-}3)$$

$$\Delta j = \nu C_{dl} \quad (3\text{-}4)$$

$$C_s = Q/\Delta E/m \quad (3\text{-}5)$$

where C_{dl} is the electrochemical double-layer capacitance of the catalytic surface, C_s is the specific capacitance of the catalysts, Δj is the difference in current variations ($\Delta j = j_a - j_c$), ν is the scan rate, ΔE is the voltage window, m is the active material mass, and Q is the charge within ΔE.[55-58] The author determined the C_{dl} value of the catalysts (Figure 3-5), whereas it is difficult to estimate the EASA owing to difficulty in determining the actual electrochemical effective mass (m) of the catalysts on the electrode.

References and Notes

1. M. K. Debe, *Nature*, 2012, **486**, 43−51.
2. Q. Li, R. Cao, J. Cho and G. Wu, *Adv. Energy Mater.*, 2014, **4**, 1301415.
3. D. Higgins, P. Zamani, A. Yu and Z. Chen, *Energy Environ. Sci.*, 2016, **9**, 357−390.
4. J. Snyder, T. Fujita, M. W. Chen and J. Erlebacher, *Nat. Mater.*, 2010, **9**, 904−907.
5. A. Rabis, P. Rodriguez and T. J. Schmidt, *ACS Catal.*, 2012, **2**, 864−890.
6. M. Shao, Q. Chang, J.-P. Dodelet and R. Chenitz, *Chem. Rev.*, 2016, **116**, 3594−3657.
7. F. Jaouen, E. Proietti, M. Lefevre, R. Chenitz, J.-P. Dodelet, G. Wu, H. T. Chung, C. M. Johnston and P. Zelenay, *Energy Environ. Sci.*, 2011, **4**, 114−130.
8. Z. Chen, D. Higgins, A. Yu, L. Zhang and J. Zhang, *Energy Environ. Sci.*, 2011, **4**, 3167−3192.
9. G. Wu and P. Zelenay, *Acc. Chem. Res.*, 2013, **46**, 1878−1889.
10. R. Bashyam and P. Zelenay, *Nature*, 2006, **443**, 63−66.
11. M. Lefèvre, E. Proietti, F. Jaouen and J.-P. Dodelet, *Science*, 2009, **324**, 71−74.
12. G. Wu, K. L. More, C. M. Johnston and P. Zelenay, *Science*, 2011, **332**, 443−447.
13. Y. Liang, Y. Li, H. Wang, J. Zhou, J. Wang, T. Regier and H. Dai, *Nat. Mater.*, 2011, **10**, 780−786.
14. Y. Nabae, M. Sonoda, C. Yamauchi, Y. Hosaka, A. Isoda and T. Aoki, *Catal. Sci. Tech.*, 2014, **4**, 1400−1406.
15. T. Ishii, T. Maie, M. Hamano, T. Kishimoto, M. Mizushiri, Y. Imashiro and J.-i. Ozaki, *Carbon*, 2017, **116**, 591−598.
16. H. Jahnke, M. Schönborn and G. Zimmermann, *Top. Curr. Chem.*, 1976, **61**, 133−181.
17. G. Lalande, R. Côté, G. Tamizhmani, D. Guay, J. P. Dodelet, L. Dignard-Bailey, L. T. Weng and P. Bertrand, *Electrochim. Acta*, 1995, **40**, 2635−2646.
18. J.-P. Dodelet, R. Chenitz, L. Yang and M. Lefèvre, *ChemCatChem*, 2014, **6**, 1866−1867.
19. Y. Hu, J. O. Jensen, W. Zhang, L. N. Cleemann, W. Xing, N. J. Bjerrum and Q. Li, *Angew. Chem. Int. Ed.*, 2014, **53**, 3675−3679.
20. U. I. Kramm, J. Herranz, N. Larouche, T. M. Arruda, M. Lefevre, F. Jaouen, P. Bogdanoff, S. Fiechter, I. Abs-Wurmbach, S. Mukerjee and J.-P. Dodelet, *Phys. Chem. Chem. Phys.*, 2012, **14**, 11673−11688.
21. N. Ramaswamy, U. Tylus, Q. Jia and S. Mukerjee, *J. Am. Chem. Soc.*, 2013, **135**, 15443−15449.
22. Q. Jia, N. Ramaswamy, U. Tylus, K. Strickland, J. Li, A. Serov, K. Artyushkova, P. Atanassov, J. Anibal, C. Gumeci, S. C. Barton, M.-T. Sougrati, F. Jaouen, B. Halevi and S. Mukerjee, *Nano Energy*, 2016, **29**, 65−82.
23. H. T. Chung, D. A. Cullen, D. Higgins, B. T. Sneed, E. F. Holby, K. L. More and P. Zelenay, *Science*, 2017, **357**, 479−484.
24. E. F. Holby and P. Zelenay, *Nano Energy*, 2016, **29**, 54−64.
25. S. Brüller, H.-W. Liang, U. I. Kramm, J. W. Krumpfer, X. Feng and K. Müllen, *J. Mater. Chem. A*,

2015, **3**, 23799−23808.
26. M. Kato, T. Murotani and I. Yagi, *Chem. Lett.*, 2016, **45**, 1213−1215.
27. Z. Zhang, S. Yang, M. Dou, J. Ji and F. Wang, *Catal. Sci. Technol.*, 2017, **7**, 1529−1536.
28. R. Zhang and W. Chen, *J. Mater. Chem. A*, 2013, **1**, 11457−11464.
29. Z. Zhang, S. Yang, M. Dou, H. Liu, L. Gu and F. Wang, *RSC Adv.*, 2016, **6**, 67049−67056.
30. R. Jiang, D. T. Tran and J. P. McClure, *RSC Adv.*, 2016, **6**, 69167−69176.
31. L. Lin, Z. K. Yang, Y.-F. Jiang and A.-W. Xu, *ACS Catal.*, 2016, **6**, 4449−4454.
32. J. Wang and F. Ciucci, *Small*, 2017, **13**, 1604103.
33. T. Tsukihara, H. Aoyama, E. Yamashita, T. Tomizaki, H. Yamaguchi, K. Shinzawa-Itoh, R. Nakashima, R. Yaono and S. Yoshikawa, *Science*, 1996, **272**, 1136−1144.
34. S. Yoshikawa, K. Shinzawa-Itoh, R. Nakashima, R. Yaono, E. Yamashita, N. Inoue, M. Yao, M. J. Fei, C. P. Libeu, T. Mizushima, H. Yamaguchi, T. Tomizaki and T. Tsukihara, *Science*, 1998, **280**, 1723−1729.
35. S. Yoshikawa and A. Shimada, *Chem. Rev.*, 2015, **115**, 1936−1989.
36. Y. Tanaka, A. Onoda, S.-i. Okuoka, T. Kitano, K. Matsumoto, T. Sakata, H. Yasuda and T. Hayashi, *ChemCatChem*, *inpress*.
37. K. Oyaizu, E. Listiani Dewi and E. Tsuchida, *Inorg. Chim. Acta*, 2001, **321**, 205−208.
38. K. I. Ansari, J. D. Grant, G. A. Woldemariam, S. Kasiri and S. S. Mandal, *Org. Biomol. Chem.*, 2009, **7**, 926-932.
39. H. C. Sampath Kumar, B. Ramachandra Bhat, B. J. Rudresha, R. Ravindra and R. Philip, *Chem. Phys. Lett.*, 2010, **494**, 95−99.
40. A. Blagus and B. Kaitner, *Acta Cryst.*, 2009, **C65**, m455−m458.
41. Y. Wang, D. C. Alsmeyer and R. L. McCreery, *Chem. Mater.*, 1990, **2**, 557−563.
42. T. Jawhari, A. Roid and J. Casado, *Carbon*, 1995, **33**, 1561−1565.
43. L. S. Panchakarla, K. S. Subrahmanyam, S. K. Saha, A. Govindaraj, H. R. Krishnamurthy, U. V. Waghmare and C. N. R. Rao, *Adv. Mater.*, 2009, **21**, 4726−4730.
44. Z. Jin, J. Yao, C. Kittrell and J. M. Tour, *ACS Nano*, 2011, **5**, 4112−4117.
45. D. Ye, S.-Q. Wu, Y. Yu, L. Liu, X.-P. Lu and Y. Wu, *Applied Physics Letters*, 2014, **104**, 103105.
46. J. Maruyama and I. Abe, *Chem. Mater.*, 2005, **17**, 4660−4667.
47. J. Maruyama and I. Abe, *Chem. Mater.*, 2006, **18**, 1303−1311.
48. M. Singh, M. Barkei, G. Inden and S. Bhan, *Phys. Status Solidi A*, 1985, **87**, 165−168.
49. P. Crespo, I. Navarro, A. Hernando, P. Rodríguez, A. G. Escorial, J. M. Barandiarán, O. Drbohlav and A. R. Yavari, *J. Magn. Magn. Mater.*, 1995, **150**, 409−416.
50. G. Pourroy, S. Läkamp and S. Vilminot, *J. Alloys Compd.*, 1996, **244**, 90−93.
51. H. Y. Chen, D. Y. Zhang and G. R. Lu, *J. Magn. Magn. Mater.*, 1990, **84**, 208−212.
52. J. R. Pels, F. Kapteijn, J. A. Moulijn, Q. Zhu and K. M. Thomas, *Carbon*, 1995, **33**, 1641−1653.
53. A. Onoda, Y. Tanaka, T. Ono, S. Takeuchi, A. Sakai and T. Hayashi, *J. Porphyrins Phthalocyanines*,

2015, **19**, 510−516.

54. A. J. Bard and L. R. Faulkner, *Electrochemical Methods: Fundamentals and Applications, 2nd Edition; New York : John Wiley & Sons*, 2001.
55. E. Gileadi, *Physical Electrochemistry: Fundamentals, Techniques and Applications.; WILEY-VCH Verlag*, 2011.
56. H. The An, T. Van Man and L. My Loan Phung, *Adv. Nat. Sci.: Nanodci. Nanotechnol.*, 2013, **4**, 035004.
57. S. K. Bikkarolla, P. Cumpson, P. Joseph and P. Papakonstantinou, *Faraday Discuss.*, 2014, **173**, 415–428.
58. J. Xie, S. Li, X. Zhang, J. Zhang, R. Wang, H. Zhang, B. Pan and Y. Xie, *Chem. Sci.*, 2014, **5**, 4615–4620.

Conclusions

The goal of this thesis is to develop the nonprecious metal catalysts with high ORR activity and high selectivity with four-electron reduction. To achieve the high activity and selectivity, the author focused on the periphery of the precursor materials, such as protein matrix and the ligand frameworks.

In the chapter 1, the author developed a high performance biomaterial-based nonprecious metal M/N/C catalyst for four-electron reduction ORR under acidic conditions. Myoglobin containing heme, an iron complex with N_4-macrocyclic cofactor, and the nitrogen-rich protein matrix was employed as a precursor. It is found that the myoglobin-based catalyst pyrolyzed at 940 ºC shows the highest ORR activity with an onset potential of 0.84 V toward efficient four-electron reduction. From this result, it is concluded that naturally available metalloproteins have a potential to be an appropriate precursor for the ORR catalysts.

In the chapter 2, the author demonstrates a new method for improving the ORR activity of Fe/N/C catalysts by introducing aromatic moieties into the structure of Fe salen precursors. The Fe/N/C catalysts prepared using the Fe complex with π-expanded ligand framework such as Fe(2NAPD) complex exhibited a remarkable positive shift (+50 mV) of the onset potential and higher selectivity for four-electron reduction ORR relative to the catalyst prepared from the simple Fe(Salen) complex. Furthermore, it is found that thermal stability of the ligand structure of precursors increases the contents of pyridinic nitrogen which forms Fe–N_4/C structures active for ORR, although the original structure of the Fe salen complexes is not remained after pyrolysis. Therefore, the Fe/N/C catalysts prepared using the Fe complex with the π-expanded ligand provide the enhanced ORR activity

In the chapter 3, the author explored to improve the ORR activity of bimetallic M/N/C catalysts employing mixed metal complex precursors with the π-expanded ligand frameworks which impart thermal stability to theirs complexes. The combination of Fe and Cu metals in the catalysts greatly enhances the ORR activity in the onset potentials with excellent four-electron reduction. Both Fe and Cu metals coordinated by pyridinic nitrogens within the catalyst surface are expected to act as efficient active sites for ORR.

In conclusion, the thesis describes the development of nonprecious metal M/N/C catalysts with high ORR activity concomitant with high selectivity for four-electron reduction by the construction of the efficient ORR active sites using the strategy tuning the peripheral chemical structures of the metal precursor materials. The author convinces that the thesis provides the significant clues for an efficient construction of ORR active sites in the M/N/C catalysts. Furthermore, the author believes that the strategy for the catalyst preparation method based on the structural design of metal complex precursors will be a

valuable guideline for the development of carbon-based heterogeneous catalysts containing nitrogen-coordinated metal active sites that promote ORR for fuel cells and other chemical reaction including OER for water electrolysis.

List of publications

1. Myoglobin-based non-precious metal carbon catalysts for oxygen reduction reaction
   Akira Onoda, Yuta Tanaka, Toshikazu Ono, Shotaro Takeuchi, Akira Sakai, and Takashi Hayashi
   J. Porphyrins Phthalocyanines, 2015, **19**, 510

2. Nonprecious-metal Fe/N/C catalysts prepared from π-expanded Fe salen precursors toward an efficient oxygen reduction reaction
   Yuta Tanaka, Akira Onoda, Shin-ichi Okuoka, Tomoyuki Kitano, Koki Matsumoto, Takao Sakata, Hidehiro Yasuda, and Takashi Hayashi
   ChemCatChem, 2017, *in press*. (front cover)

3. Bimetallic M/N/C catalysts prepared from π-expanded metal salen precursors toward an efficient oxygen reduction reaction
   Akira Onoda, Yuta Tanaka, Koki Matsumoto, Minoru Ito, Takao Sakata, Hidehiro Yasuda, and Takashi Hayashi
   RSC. Adv., 2018, **8**, 2892.